Title

Spatial ultrasonic wavefront characterization using a laser parametric curve scanning method

Authors
Chong, See Yenn
Todd, Michael D

Publication Date
2021-02-01

DOI
10.1016/j.ultras.2020.106242

Peer reviewed

Spatial Ultrasonic Wavefront Characterization Using a Laser Parametric Curve Scanning Method

See Yenn Chong[a] and Michael D Todd[a,*]
[a]Department of Structural Engineering, University of California, 9500 Gilman Drive, La Jolla, San Diego, CA 92093-0085, USA.
*Corresponding author: Email: mdtodd@eng.ucsd.edu Phone: +1(858)-534-5951

ABSTRACT

Ultrasonic wavefield imaging (UWI) provides insightful spatial information about ultrasonic wave propagation in planar (2-D) space for nondestructive evaluation and structural health monitoring (NDE-SHM) applications. In all materials, the wavefronts of the incident and reflected waves propagate with unique patterns that may be represented by parametrized polar curves in 2-D geometric space. In this paper, a spatial ultrasonic wavefront characterization method based on a parametric curve laser scan is proposed to characterize the spatial ultrasonic wavefront for both isotropic and anisotropic materials. Three parametric curves (circular, hyperbolic, and cyclic-harmonic curves) were considered. Two wavefront characterization process were carried out, namely (i) deciding the parametric equation of the closed-form geometric plane curve via UWI, and (ii) measuring and updating the ultrasound via laser ultrasonic interrogation system (LUIS) and quantifying the values(s) of the predicted parametric curve equation using a temporal cross-correlation technique. The proposed method was tested on pristine aluminum and cross-ply CFRP plates to characterize the spatial incident and reflected wavefronts of the plates. The non-fiber direction region ($105° \le \phi_S \le 165°$) and the fiber direction region ($165° \le \phi_S \le 195°$) of the cross-ply CFRP plate were considered in the test. The laser circle scan and the laser cyclic-harmonic curve scan showed the ability to characterize the incident wavefronts of the S0 and A0 modes in the aluminum plate and the CFRP plate, respectively, followed by the laser hyperbolic curve scan. With the promising results obtained in the proposed method, the integration of the parametric curve scanning method into LUIS may provide a new approach to damage detection and useful information for ultrasonic algorithm design in NDE-SHM applications.

Keywords: Ultrasonic wavefield imaging, laser parametric curve scanning, laser ultrasonic techniques, ultrasonic wavefront characterization, spatial ultrasonic wavefront pattern

1. INTRODUCTION

Ultrasonic wavefield imaging in solid media has played a significant role in ultrasonic nondestructive evaluation and structural health monitoring applications. It reveals insightful spatial information about ultrasonic wave propagation in 2-D space. Usually, laser ultrasonic techniques (LUTs) are used with a 2-D laser mirror scanner (LMS) to measure the wavefield data. The visualization of the wavefield happens by playing a sequence of 2-D spatial frames as an animated sequence. As individual images are animated, the guided waves spread outward from the source and subsequently interact with features in the target structure. Therefore, the UWI provides an excellent, high-resolution way to understand of how guided waves propagate and interact with damage such as fatigue cracks [1], impacts [2, 3], and corrosion [4].

Due to the advantages of the UWI, LUTs have been intensively designed to target isotropic metals and anisotropic composite materials [2, 5-8], owing to their non-contact nature and high spatial resolution. Since the 2-D LMS used in the LUTs is versatile, the LUTs can easily maneuver the laser beam to any desired local point to carry out the ultrasonic measurement. The most common approach used for scanning is to perform a rastering pattern over a region of interest. A circular scanning method has recently been adopted as well [9].

Nonetheless, LUTs have significant challenges in practical implementation [10, 11]. One of the challenges is slow data acquisition. Although the LUTs have the potential to conduct a large-scale structural inspection with high spatial resolution of full-field ultrasonic data, it may be impractical to perform an inspection when there is no information on the existence of damage, particularly for periodic maintenance services. A raster scan pattern is commonly used in LUTs to generate the ultrasonic wavefield in Cartesian coordinate space because it has better local damage detection. In general, however, the existing LUTs conduct the inspection process by directly performing the raster scanning without knowing whether or not there is damage. It is therefore often costly to carry out an inspection based on the raster scanning method, as the scanning time is proportional to the required inspection area. Several methods have recently been introduced to optimize the inspection time of LUTs by improving the speed of full-field ultrasonic data acquisition. The methods are categorized mainly into two approaches, optimization of LUTs hardware and optimization of laser scanning point.

In the hardware of a laser ultrasonic generator system, the speed of full-field ultrasonic data acquisition is relatively dependent on the pulse-repetition-rate (PRR) of a Q-switched laser incorporated in a laser scanning system. In Ref [12], a Q-switched laser was used and optimized with the PRR of 20 kHz. The system demonstrated the feasibility of damage detection on a CFRP plate and significantly improved the speed of the full-field ultrasonic data acquisition. However, the total length of the measurement signal was short and limited to 50 μs because the 20-kHz triggering signal of the Q-switched laser was used to synchronize with the data acquisition system (DAQ). Furthermore, the high laser scanning speed based on the in-plane regime is not suitable for the inspection of metallic structure where the reverberative field has a long dwell time. In Ref [13], the conventional laser ultrasonic system with a 2-D LMS was optimized by employing two 2-D LMSs for multi-area scanning process. Since the single laser beam of a Q-switched laser was splitted into two for the two LMSs, the power of the Q-switched laser for this configuration must be increased in order to have enough energy for the laser beam to generate an ultrasonic signal. Although this approach improved the inspection time by running the scanning process simultaneously on two different scanning areas, but this additional hardware resulted in an increase in the total cost of the laser scanning system.

Compressive sensing (CS) has recently emerged as a novel signal acquisition paradigm that allows high-dimensional signals to be reconstructed with relatively few measurements. This technique has introduced an expedition to the acquisition process of ultrasonic wavefield data [8, 14-18]. Di Ianni et al. [15] demonstrated that the signal decomposition based on the Fourier domain has better recovery accuracy with less than 34% of the original sampling grid. Harley and Chia [17] introduced a framework to use sparse wavenumber analysis based on CS [18] to create a damage-free model of the wavefield. As a result, these methods improved the scan time of current wavefield imaging. Park et al. [8] proposed an accelerated laser scanning technique based on binary search and compressed sensing to localize and visualize damage with reduced scanning points and scanning time. In any CS technique, the dictionary signal plays a key role as used to reconstruct the high-resolution signal. Thus, the signal reconstruction efficiency depends on dictionary quality. Consequently, it can take a long post-processing time and a high computational burden to obtain the "best" dictionary via a dictionary learning algorithm [19].

In addition to these two optimization approaches, the optimization of the spatial scanning pattern [9] has recently been introduced, by taking advantage of the flexibility of the laser scanning system as well as the spatial ultrasonic wavefront pattern of the material. The approach focuses on the initial process of diagnosis strategy, damage detection, for SHM applications to detect the anomalies in structures, followed by localization and then characterization (size, type, etc.). Based on this approach, the spatial circle scanning method was proposed by the authors in Ref [9]. In this work, a single circle scan was carried out by the laser scanning system to detect anomaly or damage, instead of using a full-field ultrasonic data measurement method. Since the proposed method was tested on an aluminum plate (isotropic material), the incident wavefronts (S0 and A0 modes) of the circumferential ultrasonic wave arrived at the same time in 2-D space, respectively. Due to the nature of the wave propagation pattern, the spatial ultrasonic wavefront pattern of the incident waves in the isotropic material is formed in a circular shape that can be easily characterized by a parametric circle equation. Hence, the spatial circle scanning method incorporated into the laser scanning system was able to capture the same wavefronts that were defined as a circumferential wavefront. Regards to this, the shape of the circumferential wavefront will remain intact as a circle if there is no anomaly in the directions of wave propagation, and vice versa.

Therefore, the spatial circle scanning method was developed to exploit the spatial correlation within the circumferential ultrasonic wave propagation and then find the anomaly waves response due to the damage. The covariance-variance matrix was used to evaluate the response of the correlation that acted as a feature for the damage detection. The covariance map [5] of the incident wavefronts demonstrated the ability to detect damage when the damage was located within the area of the wavefront scan point circumference. However, when the damage was located outside the area bounded by the scan circumference, the spatial correlation of the circumferential ultrasonic wave showed low defect detectability. This is because the incident wavefronts remained intact, as there was no interaction with the damage. But the reflected waves that interacted with the damage showed that the damage was still detectable.

By optimizing the spatial scanning pattern based on the spatial ultrasonic wavefront pattern in an isotropic material, the circular scanning method with the parametric circle equation demonstrated the feasibility of detecting defects. Fundamentally, this is because it is simple to characterize the spatial wavefront pattern as a circle (no circumferential variability in wave propagation). Therefore, it is much more difficult to apply the circular scanning method to an anisotropic material, e.g. a cross-ply CFRP plate, because the ultrasonic wavefront pattern is much more complex; it is unlikely to conform to a circular shape, as the wave speeds now have structured directional variability commensurate with the anisotropy. This results in variable arrival times for the incident wavefronts, resulting in decreased detection performance.

This paper hypothesizes that even with such anisotropic materials, the wavefront geometries are representable by, and similar to, parametrized polar curves in 2-D geometric space. Since the 2-D laser mirror scanner used in the system used herein [5] has the flexibility to maneuver the laser beam along any scanning curve of interest in 2-D space, this suggests that the spatial ultrasonic wavefront pattern in 2-D space may be characterized by scanning the curve in relation to a parametric curve via LUIS. To test this hypothesis, we propose a parametric curve scanning method to accomplish this. The key purpose of this new proposed method is to overcome the limitations of previous work [9] in the optimization of the spatial scanning pattern and form a generalized approach to perform an optimal scan. The following sections of this article will present the methodology of spatial ultrasonic wavefront characterization, the experimental setup for ultrasonic measurement based on the full-field scanning method and the parametric curve scanning method, and the implementation of the spatial ultrasonic wavefront characterization for incident and reflected wavefronts in both isotropic material (aluminum plate) and anisotropic material (cross-ply CFRP plate).

2. SPATIAL ULTRASONIC WAVEFRONT CHARACTERIZATION METHODOLOGY

In 2-D space, UWI provides a visualization of the propagation patterns of ultrasonic wavefronts. The spatial wavefront patterns observed can reveal important information about both the mechanics (including anisotropy leading to circumferential wave speed variability) and the possible presence of localized anomalies representing defects. Therefore, the characterization of these patterns, based on modeling them with 2-D geometric plane curves, is proposed and discussed below.

2.1 Spatial Ultrasonic Wavefront Pattern Modeling Concept

Figure 1 shows the schematic diagram illustrating the modeling concept of how the UWI's 2-D planar spatial wavefront curve may be represented parametrically. To facilitate the understanding of the concept, the UWI is generated with an artifact single sinusoidal wave propagating progressively in 2-D space at various times as shown in Fig. 1. Basically, each time frame of the UWI can be viewed as a single image describing the instantaneous state of the spatial wavefront in the *X-Y* planar domain. For example, Fig. 1 shows the spatial wavefront curve with a circular pattern emitting from the center point and growing as time evolves from t_1 to t_k (one might assume in this trivial example that the material is isotropic and homogenous). In this case the base wavefront pattern will not change as the wavefront propagates, unless there is a local impedance change or scatterer along the propagation direction. Thus, it might be reasonable to parametrize the base wavefront pattern, as in particular the wavefronts of the incident wave and reflected wave.

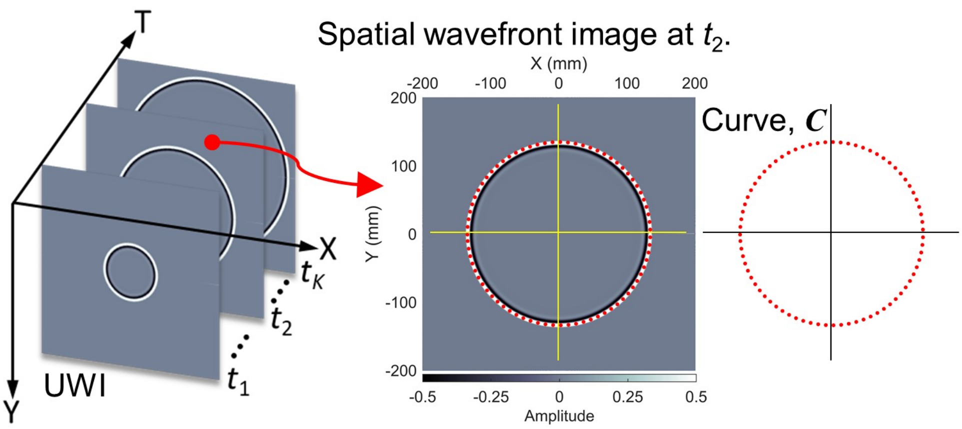

Figure 1. Modeling concept of spatial wavefront pattern parameterization.

Consider parametrizing the spatial wavefront curve at t_2 in the center of Fig. 1. Since the wavefront (red-dots in figure) is positioned at a set of coordinates (x, y) in 2-D Euclidean space ($\mathbb{R}^2$) within the *X-Y* domain, the wavefront pattern can thus be described by a planar curve (***C***) as shown the right-hand-side of Fig. 1, generally described as

$$\boldsymbol{C}(\beta) = \{(g(\beta), h(\beta)) : \beta \in I\}, \quad (1)$$

by mapping the parameter $\beta \in \mathbb{R}$ to a point $\boldsymbol{C} \in \mathbb{R}^2$ on the curve, ranging over an interval *I*. The coordinate (x, y) of the circular wavefront are defined as functions of an independent parameter β, i.e., $x = g(\beta)$ and $y = h(\beta)$, which are the parametric equations describing a planar curve. Consequently, a spatial wavefront pattern with a set of coordinates (x, y) can be characterized and modeled in a parametric equation when the parameter β is determined for an interval I. To realize this modeling concept, a spatial ultrasonic wavefront characterization process using a laser ultrasonic technique is introduced and discussed next.

2.2 Spatial Ultrasonic Wavefront Characterization Process

Figure 2 shows the flowchart of the spatial ultrasonic wavefront characterization process for the 2-D spatial wavefront using the laser parametric curve scanning method. In other terms the ultrasonic wavefront patterns in 2-D space are characterized and defined by the 2-D geometric plane curve parametric equation introduced above. The blue box and the red box in the flowchart are the procedures performed in Matlab^{TM} 2019b software and LUIS, respectively. The characterization process is composed of two primary processes. The first process, named Process 1, at the left-hand side of the flowchart is to decide the closed-form geometric plane curve that describes the wavefront patterns. The second process, named Process 2 at the right-hand-side of the flowchart, is to measure the ultrasound through the LUIS with the parametric curve equation obtained form Process 1 and quantify the accuracy of the wavefront characterization by updating the parameter(s). The process of the parameter(s) updating is repeated until the desired parameter(s) value(s) of the parametric curve equation is(are) reached. The implementation of the proposed method in Fig. 2 does not require two independent platforms (Matlab^{TM} software and LUIS), as they may be easily integrated into the LUIS platform, but that is beyond the scope of this paper.

The UWI plays a significant role in the characterization process. It provides prior knowledge of the spatial ultrasonic wavefront pattern and the geometric plane curve in relation to the incident and reflected waves of a specimen. Basically, the formation of the spatial ultrasonic wavefront pattern depends on the velocity of the ultrasonic guided waves (Lamb waves) in a plate-like structure, which in turn depends on the material properties and frequency-thickness product. The material of the specimen may be either a metallic (isotropic material) or a composite (anisotropic/quasi-isotropic material). The fundamental symmetric (S0) and asymmetric (A0) modes of Lamb waves are frequently considered in these materials for NDE-SHM applications. So, the characterization process suggested in Fig. 2 focuses only on the incident wavefronts of these two fundamental modes and the reflected wavefronts at a selected frequency range. The frequency range can be either narrowband or broadband, which can be easily done with a signal-condition device as incorporated into LUIS, described in section 3.1. The separation of these two modes in 2-D space must be achieved first so that the S0/A0 mode may be characterized with the right parameter values. To do so, the size of the specimen must be large enough to allow these two modes to have enough time to separate during the wave propagating in 2-D space. Since the velocity of the Lamb waves in a plate-like structure depends on the thickness of the plate, the plate must therefore be relatively flat unless the characterization process is intentionally performed to parameterize the wavefront pattern of a plate with varying thickness. For composite plates, the placement accuracy from local fiber stacking variations can also affect the accuracy of the characterization performance. Finally, when the incident wave of the S0/A0 mode reflects at a plate boundary, the reflected pattern correlates to the shape of the boundary; the boundary shape is assumed to be utilized as prior knowledge in order to inform the characterization process for parameterizing the reflected wave portion. Consequently, the dependent factors for the characterization process can be summarized as (i) material types, (ii) wavefront types, (iii) plate-like geometric settings (size, thickness, boundary), and (iv) frequency range, where these settings must be clearly defined before starting the characterization process.

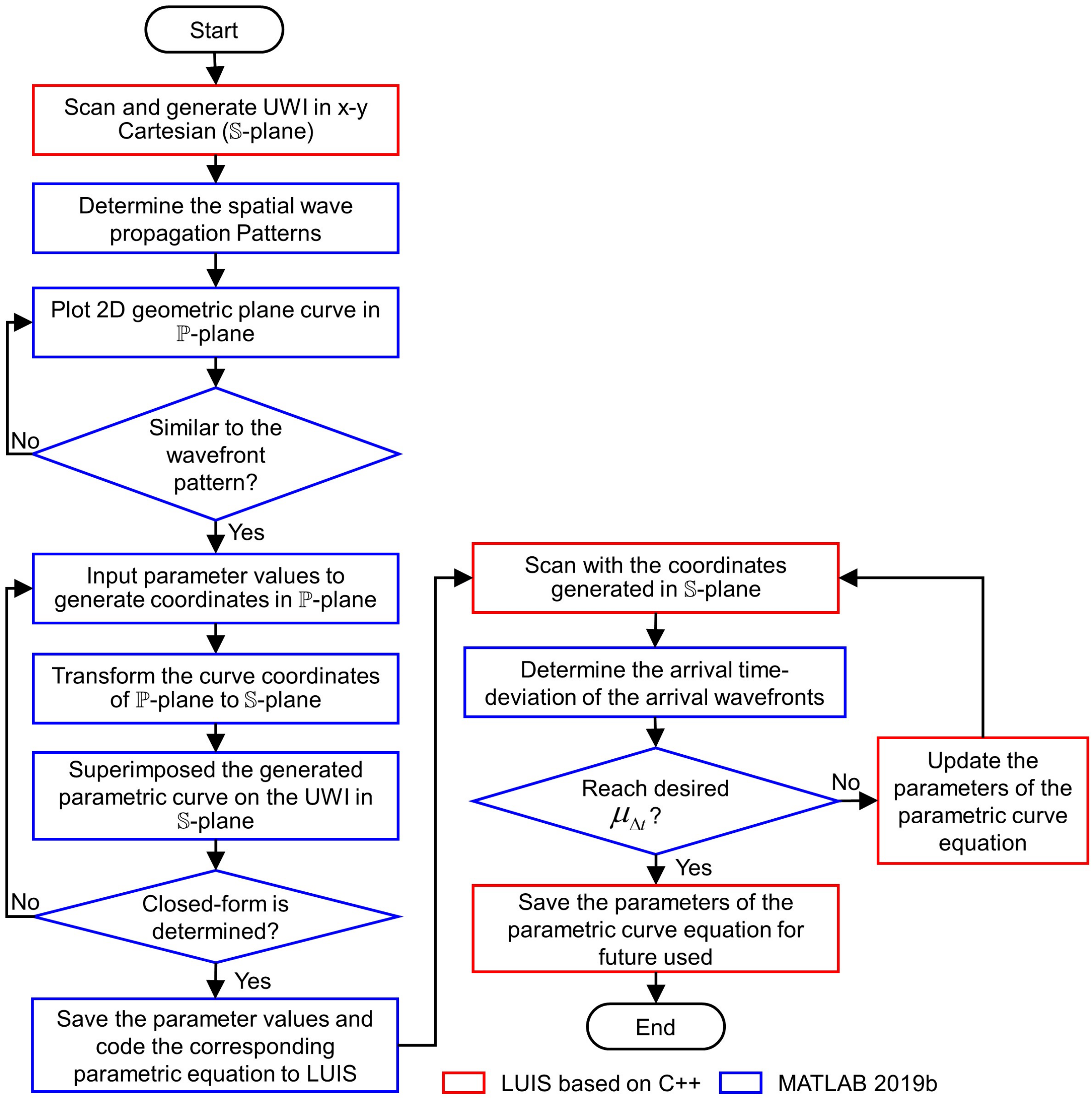

Figure 2. Flowchart of spatial ultrasonic wavefront characterization process. ($\mu_{\Delta t}$: mean arrival time-deviation)

The method of characterization in Fig. 2 is implemented with the objective of constructing a database containing the various sets of parametric equations of the spatial ultrasonic wavefront pattern relative to materials that ultimately provide a resource for NDE-SHM applications. Furthermore, with this database, a user may search whether for a particular spatial ultrasonic wavefront pattern corresponding to a particular material design. If the database does not have the details, the user would then have to carry out characterization process as shown in Fig. 2 in order to create new parametric equation(s) for the spatial ultrasonic wavefront of a plate-like structure with the initial settings based on the dependent factors.

Process 1: Identification of Closed-form Curve

Consider the creation of a new parametric equation for a spatial ultrasonic wavefront pattern of a plate-like specimen. The dependent factors' settings of the specimen are defined, and LUIS starts performing the full-field ultrasonic measurement to generate the UWI. The experimental setup with LUIS will be discussed in section 3.1. Once the measurement process is completed, the UWI of the specimen is generated and represented in the three-dimensional (3-D) volume data with 3-D spatial-temporal domain as shown in Fig. 1. Each UWI time frame (slice) is represented as a 2-D spatial wavefront image in the X-Y planar domain (described in this paper as $\mathbb{S}$-plane), with the horizontal and vertical axes of x and y respectively. Hence, with the spatial wavefront image at a time instant t, the geometric plane curve associated with ultrasonic wavefront pattern may be identified in the $\mathbb{S}$-plane as shown in the center of Fig. 1.

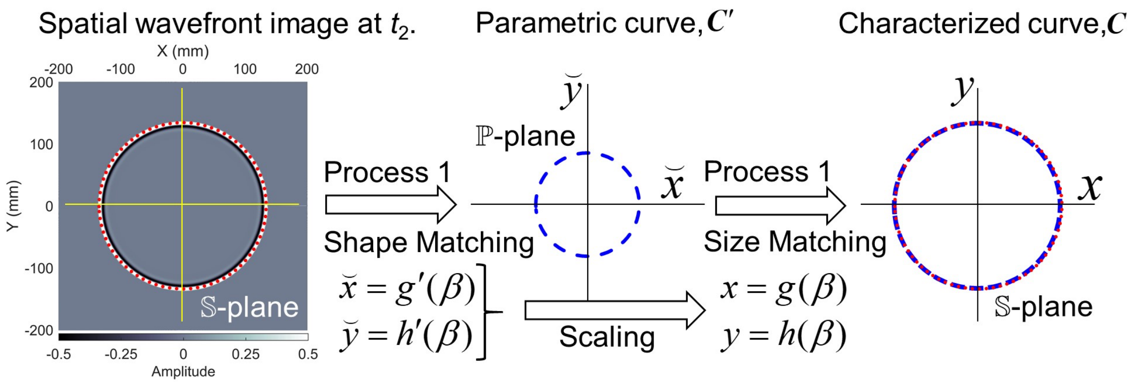

Figure 3. Spatial ultrasonic wavefront characterization – Process 1.

After deciding the targeted spatial wavefront, e.g., the incident wavefront in the spatial wavefront image at t_2 in Fig. 3, the shape matching process is carried out first in Process 1. The shape matching process is to match the shape of the parametric curve (blue-shaded circle in the center of Fig. 3) to the planar curve (red-dots in the left-hand side of Fig. 3) associated to the desired wavefront pattern in the spatial wavefront image. Various fundamental geometric curves have been studied [20, 21] with well-defined parametric equations. The incident and reflected wavefront patterns of Lamb waves in a plate-like structure show very reasonable association with these basic parametric curves (e.g. circle, hyperbola, etc.). Therefore, the shape matching processing can be carried out easily using these basic parametric curves with the spatial wavefront pattern. The parametric equations and curves are discussed further in section 3.2.2. Of course, when the complexity of the wavefront pattern is substantially increased (particularly in reflection patterns in geometrically complex anisotropic structures), they may not have a corresponding fundamental parametric equation, but parametrization of the wavefront pattern may still be performed by using a parametric curve fitting method [22, 23]. The complexity of the wavefront pattern is highly affected by local impedance changes or scattering conditions (e.g. crack, lap-joints, etc.), but the current paper does not consider how the present method might be used in defect detection.

Thus, the parametric curve (blue-shaded circle) can be identified based on the planar curve (red-dots) on the desired wavefront pattern in the left-hand side of Fig. 3. The corresponding parametric equations are then determined and expressed as $\breve{x} = g'(\beta)$ and $\breve{y} = h'(\beta)$ with the parameter β. Subsequently, the predicted parametric curve $\boldsymbol{C}'$ with the coordinates $(\breve{x}, \breve{y})$ in the 2-D-plane is generated and plotted as shown in the center of Fig. 3. The 2-D-plane is defined as ℙ-plane in this paper with the horizontal and vertical axes of $\breve{x}$ and $\breve{y}$ respectively. Basically, in this stage, the parametric curve plotted in the ℙ-plane is employed as a shape reference to assess the shape similarity to the desired wavefront pattern in 𝕊-plane regardless of the size of the desired wavefront pattern. For that, the coordinates $(\breve{x}, \breve{y})$ are unitless and generated under the range of $-1 \le \breve{x} \le 1$ and $-1 \le \breve{y} \le 1$ in ℙ-plane. If the predicted parametric curve shows a weak resemblance to the desired wavefront pattern, then the shape matching process will repeat and reassesses the desired wavefront pattern with another type of parametric curve.

After making a match to a target fundamental curve, the next step is to alter the size of the predicted parametric curve to match the size of the desired wavefront pattern. The two are depicted in separate planes, the ℙ-plane and 𝕊-plane as shown in Fig. 3, with different units. Consequently, to execute the size matching operation, the parametric equations of the predicted parametric curve $\boldsymbol{C}'(\beta)$ in the ℙ-plane need to be rescaled to the 𝕊-plane as expressed below

$$x = g(\beta) = \alpha_x g'(\beta) \quad \text{and} \quad y = h(\beta) = \alpha_y h'(\beta), \tag{2}$$

where the α_x and α_y are the scale factors of x and y, respectively. Therefore, a new curve $\boldsymbol{C}(\beta)$ can be obtained based on the new parametric equations (Eqn. (2)). This new curve $\boldsymbol{C}(\beta)$ is called a "characterized curve" in this paper. The parametric equations of the characterized curves, which are corresponding to the incident and reflected waveforms, will be discussed in section 3.2.2. Of course, the size of the incident wavefront increases as it emanates from a point source; nonetheless, the originating pattern of the ultrasonic wavefront will not change, subject to the restrictions above (no local strong defects or other major scatters, for example). The same is true of the reflecting wavefront, although the geometric effects at the boundary will have induced a fundamental change compared to the incident waves, but this will be considered later. Thus, during the matching process, the values of the scale factors of x and y will be altered to fit the wavefront size without altering the expression of the predicted parametric curve ($\boldsymbol{C}'$). When each time the scale values are modified, the new corresponding coordinates (x, y) of the characterized curve are produced. The characterized curve (blue-shaded circle in the right-hand side of Fig. 3) is then superimposed on the desired wavefronts (red-dots) in the $\mathbb{S}$-plane. This superimposition method is performed to serve as a benchmark for determining the values of the corresponding scale factors of the parametric equation of the characterized curve.

As illustrated in Fig. 2, if the characterized curve is not matched to the target patterns, the procedure is repeated by adjusting the parameter(s) value(s) accordingly until the shape and size of the characterized curve is matched to some tolerance. If the size of the curve $\boldsymbol{C}(\beta)$ (blue-shaded circle in the right-hand side of Fig. 3) is matched to the planar curve (red-dots) of the desired spatial ultrasonic wavefront pattern, it thus means that the spatial wavefront pattern with the set of coordinates (x, y) is characterized and modeled in the parametric equation (Eqn. (2)) when the parameter β is determined for an interval *I*. Lastly, the characterized curve is obtained based on this predicted parametric curve equation with the corresponding parameter value(s) and scale factors.

Process 2: Quantification of Parameterization

After the characterized curve is obtained, the corresponding predicted parametric equations with the value(s) of the parameter(s) are saved for future reference and coded into LUIS. Using the value(s) of the parameter(s) obtained in Process 1, the LUIS generates the coordinates (x, y) of the characterized curve and runs the scanning process on the specimen. LUIS performs a pixel scanning order that exactly matches the characterized curve obtained in Process 1, which is of course the same as the target spatial wavefront to be characterized by the spatial ultrasonic wavefront image. During the scanning process, each local ultrasonic signal is measured accordingly along the curved scanning path, and the measurements are then used to quantify the accuracy of the characterization process based on the arrival times of the desired spatial wavefronts.

In general, the type of laser used in LUTs employed for scanning may be either a laser pulse, acting as an actuator (ultrasonic generator), or a laser Doppler vibrometer (LDV), acting as a sensor (ultrasonic receiver). In this paper, LUIS exploits a laser pulse as an ultrasonic generator and a PZT-based sensor as an ultrasonic receiver for Process 2 in the characterization process, but the current approach is not specific to LUIS' architecture; more information on the specific LUIS configuration will be addressed in section 3.1. Based on this selected configuration of LUIS, multiple ultrasonic signals are generated along the characterized curve (***C***) path and then received at the PZT-based sensor. Usually, the sensor is located at the center of the plate and inside the area bounded by the characterized curve so that maximal lines of sight are maintained.

When the matched parametric curve scanning process is completed, the measurement set, defined as $u(\theta_{\mathbb{S}}, t)$, is reconstructed in the angle-time domain and depicted in a 2-D image with $M \times N$ grid points, indexed by an angle $\theta_{\mathbb{S}}$ (horizontal-θ-direction) and a time t (vertical-direction) respectively. The angle $\theta_{\mathbb{S}}$ is the propagation direction of the measured ultrasonic waves relative to a sensor located at the center point in the $\mathbb{S}$-plane. Each ultrasonic signal $u(\theta_{\mathbb{S}}, t)$ is digitized at a sampling angle $\Delta\theta_{\mathbb{S}}$ and a sampling time T_S during the measurement in LUIS. The digitized ultrasound $u(\theta_{\mathbb{S}}, t)$ is thus referred as $u[m, k]$, where m is an index that assigns a number to each angle sample $\theta_{\mathbb{S}}$, ranging from 1 to M in θ-direction, and k is an index that assigns a number to each time sample t, ranging from 1 to N. The sample angle $\theta_{\mathbb{S}}$ is then expressed as $\theta_{\mathbb{S}} = m\Delta\theta_{\mathbb{S}}$ and the sample time t is expressed as $t = kT_S$. The sample angle and the sample time are then simply represented as m and k, used subsequently in the rest of the paper. The 2-D image representing the $u(\theta_{\mathbb{S}}, t)$ or $u[m, k]$ in the angle-time domain is known in this paper as a parameterized ultrasonic wavefront image (PUWI).

To summarize the proposed process, any wavefront propagates in a plate-like structure with either a constant wave speed (isotropic material) or a direction-dependent wave speed (anisotropic material). The pattern of the spatial wavefront that forms is unique to that material and is identifiable in the spatial ultrasonic wavefront image as shown in Fig. 1. A snapshot in time, as in Fig. 1, corresponds to a radial direction time-of-arrival time for that locus of points. For example, as shown in Fig. 4, the same spatial wavefront (green dots) arrives at the same (t) in 2-D space for all the propagation directions. Since it is an isotropic material, as shown in Fig. 4(a), the ultrasonic signals, u_1 and u_2 in the 2-D space travel at the same speed (v) and arrive at time t with the same radius (r). But, in the anisotropic material as shown in Fig. 4(b), the u_3 and u_4 in the 2-D space travel at the different speeds (v_3 and v_4) and arrive at time t with different radii (r_3 and r_4). This shows that if the radius of the same spatial wavefront in the spatial ultrasonic wavefront image (independent of material) is estimated correctly, the arrival time of the corresponding wavefront will then be the same for all the propagation directions. And, as mentioned in Process 1, this spatial wavefront is characterized and represented into a set of coordinates (x, y) which relate to these radii.

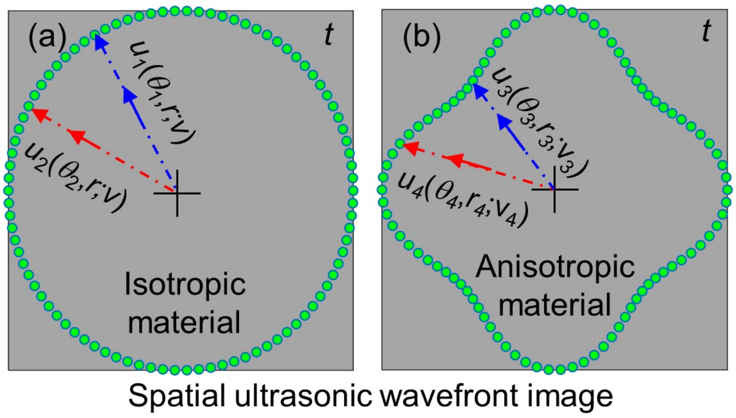

Figure 4. Spatial ultrasonic wavefront images at a time instant *t* for (a) isotropic and (b) anisotropic materials.

Therefore, the similarity of the laser parametric scanning curve on the specimen to the pattern of the spatial ultrasonic wavefront at a given time instant reflects the accuracy of the approach. And as such, if the laser scans with the characterized curve that precisely marks the same spatial wavefront positions, the resulting arrival times are the same, and the arrival time-deviation in all the propagation direction is zero. Hence, the mean arrival time-deviation ($\mu_{\Delta t}$) of the measured spatial wavefront (IWs and RWs) for an angle range (from $\theta_{\mathbb{S}}^{\min}$ to $\theta_{\mathbb{S}}^{\max}$) is calculated to evaluate the similarity of the characterized curve to the actual spatial wavefront pattern. The subscript Δt is referred to as the arrival time-deviation at an angle $\theta_{\mathbb{S}}$ with the condition of $\theta_{\mathbb{S}}^{\min} \le \theta_{\mathbb{S}} \le \theta_{\mathbb{S}}^{\max}$. If the $\mu_{\Delta t}$ is not reached or is larger than the desired preset value (ideally is zero), then the characterized curve pattern has no clear resemblance to the pattern of the spatial wavefront. Consequently, the smaller the obtained $\mu_{\Delta t}$, the more accurate the parameter value(s) estimated.

To calculate $\mu_{\Delta t}$, a temporal cross-correlation technique is employed to calculate the arrival time-deviation Δt by cross-correlating the reference signal with the test signals. In this paper, the reference signal is set to the measured ultrasonic signal at the angle range center. The corresponding $\theta_{\mathbb{S}}^{\min}$ and $\theta_{\mathbb{S}}^{\max}$ are denoted as $m_{\min}$ and $m_{\max}$ with the conditions of $1 \le m_{\min} \le M$ and $1 \le m_{\max} \le M$. Then, the discrete-time cross-correlation is expressed as below:

$$C[m,\tau] = \sum_{k=k_{\min}}^{k_{\max}} u_{\mathrm{Ref}}[m_{\mathrm{Ref}}, k]\, u[m, k+\tau], \quad 0 \le \tau \le K-1 \tag{3}$$

Where τ is the lag, and $u_{\mathrm{Ref}}[m_{\mathrm{Ref}}, k]$ and $u[m,k]$ are the reference signal and the test signal, respectively. The test signal is the measured ultrasounds as plotted on the PUWI. The m is bounded as $m_{\min} \leq m \leq m_{\max}$, and m_{Ref} is equaled to the center index value between $m_{\min}$ and $m_{\max}$. Since the PUWI provides high visibility of the wavefront propagation in the 2-D angle-time domain, the time window ranging from $t_{\min}$ and $t_{\max}$ are defined as $k_{\min}$ and $k_{\max}$ respectively, and implemented in Eqn. (3).

Once the $C[m,\tau]$ is acquired, the arrival time-deviation $\Delta t[m]$ can be determined by the maximum argument of $C[m,\tau]$,

$$\Delta t[m] = \arg\max_{\tau} \left\{ C[m,\tau] \right\}, \quad m_{\min} \leq m \leq m_{\max}, \tag{4}$$

and subsequently, the $\Delta t[m]$ is used to determine the mean arrival time-deviation $\mu_{\Delta t}$, or

$$\mu_{\Delta t} = \frac{1}{M} \sum_{m_{\min}}^{m_{\max}} \Delta t[m]. \tag{5}$$

If the mean arrival time-deviation is calculated and deemed unsatisfactory for any reason, the similarity refining process will be repeated by updating the parameter values of the characterized curve equation. The refining process is carried out manually in this paper, but the process could be automated with a robust optimization technique in the future. Lastly, when the desired $\mu_{\Delta t}$ is obtained, the corresponding parameter(s) value(s), and the characterized curve equation are all stored to the LUIS for future reference, which may be of benefit to NDE-SHM applications. To align with the motivation of this paper, the parametric curve equation obtained in this characterization process may eventually be used to improve the laser ultrasonic inspection time based on the spatial scanning optimization approach for other materials, especially anisotropic material structure.

3. IMPLEMENTATION OF SPATIAL WAVEFRONT CHARACTERIZATION METHOD

3.1 Experimental Setup

A laser ultrasonic interrogation system (LUIS) described in detail previously [9] was again configured to perform the scanning on both an aluminum plate (isotropic material) and a cross-ply CFRP plate (anisotropic material) with the stacking sequence of $[0°/90°/0°]_S$. The dimensions of the aluminum plate and the CFRP plate were 457.2 mm (H) × 508.0 mm (W) × 3.1 mm (T) and 500.0 mm (H) × 504.0 mm (W) × 1.2 mm (T), respectively.

Two experiments were carried out in this paper. One was performed to measure the propagation of the full-field ultrasonic wave for the generation of UWI based on the full-field scanning method; the other was performed to measure the propagation of the ultrasonic wave for the generation of PUWI based on the parametric curve scanning method. During the scanning process, the pulse repetition rate (PRR) of the LUIS was set to 50 Hz and 1 kHz to measure the aluminum plate and the CFRP plate respectively. Since the attenuation coefficient of the aluminum plate is lower than the CFRP plate, the PRR was set 50 Hz for the aluminum plate to avoid reverberation interference during the scanning process. Each generated ultrasound was propagated from the local scan point and received at the piezoelectric (PZT) sensor (S1) which located at the center of the rear scanning surface. The data acquisition system then digitized each local ultrasound. The sampling time for the aluminum and CFRP plates was set to $T_S = 0.2\,\mu\text{s}$ (5 MHz) with total sample points K = 1000 and K = 2000, respectively.

Since both specimens had not been characterized as described in Process 1, the measurement of the full-field ultrasonic wave propagation must be executed first to generate UWI for use in the closed-form curve identification process. For both aluminum and CFRP plates, the in-line bandpass filter was set at 50 kHz low-cutoff frequency and 500 kHz high-cutoff frequency. Circle scanning was used for the full-field measurement instead of raster scanning. The radius was set at the radius interval Δr = 0.5 mm from 20 mm to 220 mm and the angle $\theta_{\mathbb{S}}$ was at the angle interval $\Delta\theta_{\mathbb{S}} = 0.13°$ from 0° to 360°. After the scanning process was completed, the full-field ultrasonic data in polar coordinates with $r \times \theta \times t$ matrix grids was converted into Cartesian coordinates with $X \times Y \times t$ matrix grids as shown in Figs. 5 and 6. Because the ultrasonic measurement was performed at the high-resolution scanning angle interval (0.13°) in this paper, there should be no significant variations between the UWI obtained in this circle scanning method and the UWI obtained based on the raster scanning method.

The LUIS carried out the parametric curve scanning process in Process 2 based on the results of the characterized curve obtained from in Process 1 as shown in Figs. 2 and 3. Two frequency bands of the measured ultrasounds were considered for both plates at 50-500 kHz (broadband) and for only the CFRP plate at 140-150 kHz (narrowband). The implementation of the proposed method (spatial ultrasonic wavefront characterization) is carried out in the next section, and the related findings are evaluated and discussed.

3.2 Process 1 – identification of Closed-form Curve

3.2.1 Spatial Ultrasonic Wavefront Patterns

Based on the flowchart (Fig. 2), the UWI generation is a requirement that must first be considered when the characterized curve of the desired wavefront is not available in the database. So, the ultrasonic wavefront patterns for the closed-form curve recognition process can be identified by taking advantage of the UWI.

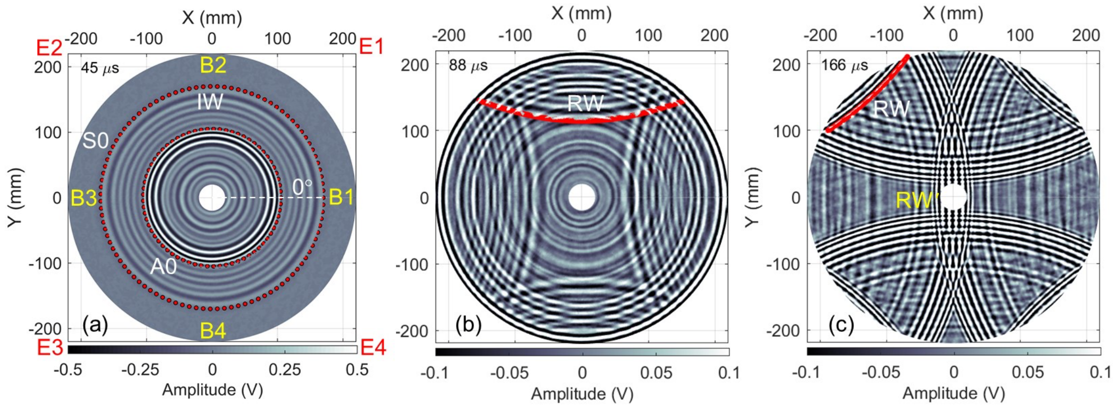

Figure 5. Spatial ultrasonic wavefront images of 3-mm thick aluminum plate at (a) 45 μs, (b) 88 μs, and (c) 166 μs.

As stated in section 3.1, the experimental setup for the full-field ultrasonic measurement was performed to produce the UWIs of the aluminum and CFRP plates, respectively. Figures 5 and 6 show the spatial ultrasonic wavefront images of the aluminum plate UWIs and the CFRP plate, respectively, in $\mathbb{S}$-plane. Assuming that reciprocity holds in this linear elastodynamic system [11], the ultrasonic waves are visualized as the wavefronts emanate over time from a sensor ("acting" as a point-source). Consequently, Figs. 5(a) and 6(a) show the IWs radially propagated out from the sensor S1 at the center point (0, 0) in the spatial wavefront image for all propagation directions. As both the plates were pristine, only the RWs were observed, which were induced at the boundaries and corners of the plates after the fastest IWs reflected. Commonly, the fastest IW is the fundamental symmetric Lamb mode (S0) followed by the fundamental anti-symmetric Lamb mode (A0) as indicated in Fig. 5(a).

At Fig. 5(a), the IWs (red-dotted circles) of the S0 and A0 modes propagated in the aluminum plate in a circular wavefront pattern. The circular wavefront pattern was shaped since each mode traveled from the sensor S1 at the same wave velocity in all propagation directions. As the S0 mode's wave velocity is faster than the A0 mode, the S0 and A0 mode's arrival distance is different at any time instant. Therefore, the IWs of the S0 and A0 modes arrived at a separate distance 170 mm and 105 mm respectively at the time instant 45 μs (Fig. 5(a)).

Then, the RWs induced by the S0 mode were created at 88 μs (Fig. 5(b)) from the boundaries B1, B2, B3, and B4. The B1 and B3 RWs were closer to the S1 (0, 0) than the B2 and B4 RWs because the aluminum plate shape was rectangular, which the B2 and B4 lengths were shorter than the B1 and B3 lengths. Figure 5(c) also shows the RWs induced by A0 mode traveling at 166 μs from the four corners E1, E2, E3, and E4 to the S1. The spatial wavefront image also displayed the reflected wavefronts from B1 (referred to as RW′ in Fig. 5(c)) passing through the S1 and moving to B3 when the time of ultrasonic measurement was long enough. It is found that the RWs' wavefront patterns from the borders and corners were shaped in patterns of hyperbolic wavefronts.

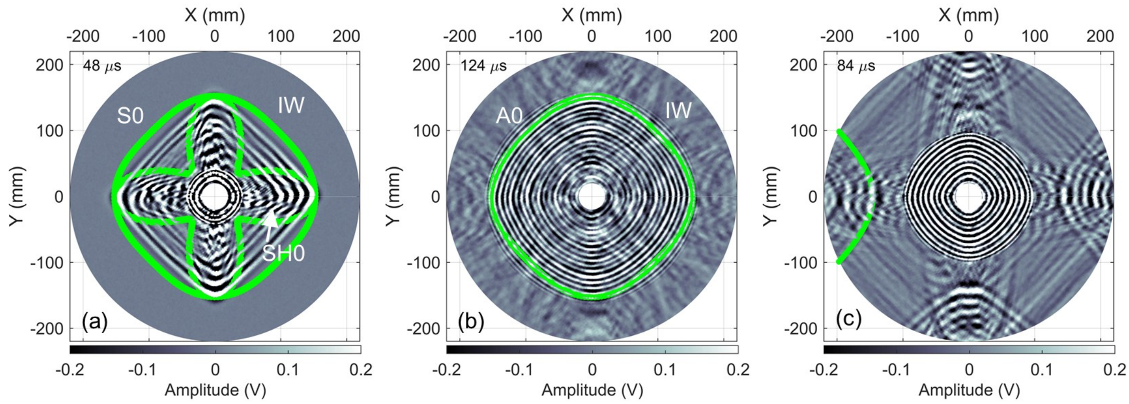

Figure 6. Spatial ultrasonic wavefront images of cross-ply CFRP plate at (a) 48 μs, (b) 124 μs, and (c) 84 μs.

Figure 6 shows the spatial ultrasonic wavefront images of the cross-ply CFRP plate ([0°/90°/0°]s). The CFRP plate is an anisotropic material with the directional-dependent physical properties that cause directional variation in guided wave propagation in space. Thus, as shown in Fig. 6(a), the wavefront patterns of the CFRP plate are (not surprisingly) more complex than the wavefront patterns of the aluminum plate for all the propagation directions. In Figs. 6(a) and (b), the wavefronts of the fundamental Lamb wave modes (S0, A0, SH0) were observed. The S0 mode had the highest wave velocity, and the A0 mode had the lowest. The SH0 mode was identified in the spatial wavefront image as well as between the S0 mode and A0 mode as shown in Fig. 6(a). Figures 6(a) and (b) show that the IWs (green-dots curves) of the S0 and A0 modes were propagated with the cyclic-harmonic curve patterns. The RWs propagated in the hyperbolic patterns (Figs. 6(c)) similar to the RWs in the aluminum plate.

The wavefront patterns in the spatial ultrasonic wavefront image were identified by reference to the above observation. The circle curve was found in the aluminum plate and was similar with the IWs. As for the CFRP plate, it found also that the cyclic-harmonic curve was identical to the IWs. On the other hand, the hyperbolic curve from the boundaries and corners of both plates was found identical to the RWs. Based on these observations, the description of the parametric curve equations of these described wavefront patterns (Figs. 5 and 6) were discussed next to obtain the characterized curves for the IWs and RWs.

3.2.2 Parametric Plane Curves

In this sub-section, the cyclic-harmonic curve is described first for the IWs of the S0 and A0 modes in both aluminum and CFRP plates. Then, the hyperbolic curve is described for the RWs.

Cyclic-harmonic Curve (CHC)

The parametric equation of cyclic-harmonic curve is selected for the parametric curve for the wavefronts patterns of the S0 and A0 modes in both aluminum and CFRP plates; and the corresponding parametric equation of CHC in $\mathbb{P}$-plane is expressed as

$$\breve{x} = \frac{\cos(\theta_{\mathbb{P}})}{1+p}\left(1 + p\cos(n\theta_{\mathbb{P}} + \varphi)\right) \quad \text{and} \quad \breve{y} = \frac{\sin(\theta_{\mathbb{P}})}{1+p}\left(1 + p\cos(n\theta_{\mathbb{P}} + \varphi)\right), \tag{6}$$

where n is a number set to the total number of petals in a CHC. The petal is the based pattern of the CHC. The base pattern of the petal is also can be changed by setting the parameter p and the phase φ. The phase φ is defined as the rotation angle of the CHC.

As stated in previous section 2.2, to obtain the parametric equation of the characterized curve, the unitless shape of the parametric curve $\boldsymbol{C}'$ must be predicted first. Thus, based on the circular form of the S0 and A0 modes' IWs in the aluminum plate, as illustrated in Fig. 5(a), the corresponding parametric equation in $\mathbb{P}$-plane was found by setting the p to zero in Eqn. (6) and the expression can be simply expressed as

$$\breve{x} = \cos(\theta_{\mathbb{P}}) \quad \text{and} \quad \breve{y} = \sin(\theta_{\mathbb{P}}), \tag{7}$$

where the $\breve{x}$ and $\breve{y}$ are the coordinates of the unit circle with the angle $\theta_{\mathbb{P}}$ ranging from 0° to 360° in the $\mathbb{P}$-plane. Subsequently, the size of the circle shape is matched to the IWs in $\mathbb{S}$-plane by fitting the scale factor to obtain the coordinates (x, y) of the characterized curve with the expression

$$x = R \cdot \breve{x} \quad \text{and} \quad y = R \cdot \breve{y} \tag{8}$$

where, the R is the scale factor and it is a radius as defined in $\mathbb{S}$-plane for the desired IW. Then, the resulting circle is drawn on the desired IWs in the $\mathbb{S}$-plane to match the size of the produced circle with the desired IWs in $\mathbb{S}$-plane.

In this work, the spatial ultrasonic wavefront image at 45 μs (Fig. 5(a)) was considered, and at this time the IWs of the S0 and A0 modes arrived at the radius of 170 mm and 100 mm respectively. For this, the radii of R = 170 mm and R = 100 mm were set separately into Eqn. (8) to generate two different coordinates (x, y) of the circles respectively with the values of $\breve{x}$ and $\breve{y}$ obtained from Eqn. (7). The circles (red dots) were then drawn at 170 mm over the IW of the S0 mode and at 100 mm over the A0 mode as shown in Fig. 5(a). Figure 5(a) demonstrated that, at the desired radius, the characterized curves fit well with the IWs of the S0 and A0 modes.

In the case of the aluminum plate, the characterized curve obtained in Process 1 is simple, where the parametric equation requires only the parameter $\theta_{\mathbb{P}}$ and the scale factor, R, to be considered in this paper. Next, the characterized curves at the R (170 mm and 100 mm) and the corresponding parametric equations (Eqns. (7) and (8)) were coded and stored for Process 2 to further quantify the similarity of the characterized curve to the desired spatial wavefront pattern. Process 2 implementation will be described further in section 3.3.

Next, as shown in the wavefront patterns in the CFRP plate (Figs. 6(a) and (b)), the cyclic-harmonic curves (Figs. 7(a) and (b)) are selected as the parametric curves for the wavefronts patterns of the S0 and A0 modes. Figure 7(a) shows that the CHC is revolved at the counterclockwise direction (arrows from 1 to 8) with four petals (n = 4) at φ = 0. The curve, for $0 < p < 1$, is converged at an offset distance from the (0, 0) when the $\theta_{\mathbb{P}}$ at ±45° and ±135° as shown in Fig. 7(a).

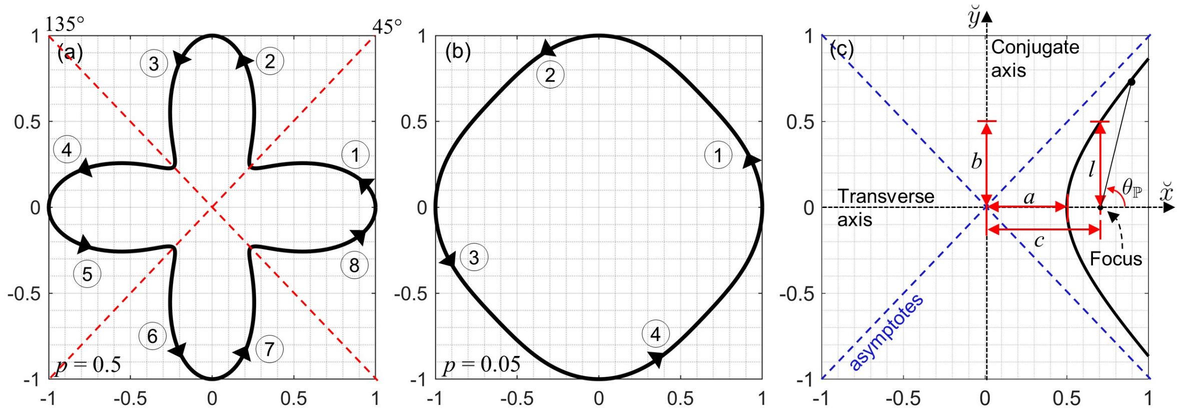

Figure 7. Parametric plane curves of cyclic-harmonic curve ((a) p = 0.5 and (b) p = 0.05)) and (c) hyperbolic curve on the $\mathbb{P}$-plane.

By observing Fig. 6(a), the IWs of the S0 mode in the cross-ply CFRP formed patterns like the shapes in Figs. 7(a) and (b). Figure 7(a) shows that the CHC at p = 0.5 has a strong resemblance to the IWs of the S0 mode in the fiber direction region (Fig. 6(a)). On the other hand, Fig. 7(b) shows that the CHC at p = 0.05 has a strong resemblance to the IWs of the S0 mode in the non-fiber direction region (Fig. 6(a)). Then, Fig. 7(b) also shows that the CHC at p = 0.05 has the strong resemblance to the IWs of the A0 mode in non-fiber and fiber direction regions (Fig. 6(b)). As a result, in the next step, the CHC as defined in Eqn. (6) was further used to match the size in Figs. 7(a) and (b) to the size of the IWs of the S0 and A0 modes in Figs. 6(a) and (b) to obtained the characterized curve respectively.

To match the size of the CHC to the size of the desired IWs, the coordinates (x, y) of the characterized curve in $\mathbb{S}$-plane can be generated by using Eqn. (8), except that the $\breve{x}$ and $\breve{y}$ obtained from Eqn. (6) are substituted into Eqn. (8). The radius R of Eqn. (8) is then referred to as the distance between the center point of the plate and the peak points of the petal at ±90° and ±180° in the $\mathbb{S}$-plane.

Commonly, a parametric curve equation may be expressed with multiple parameters, like this case. To ease the confusion, the parameters and scale factors are grouped into a set, denoted as $\mathbf{P}\{\bullet\}$. Then, $\{\bullet\}$ is the elements of the set representing the parameters and scale factors of the characterized curve equation. Therefore, the parameters (n, p, φ) and scale factor (R) of the characterized curve are written as $\mathbf{P}_{\text{CHC}}\{n, p, \varphi, R\}$ with the angle range of $0° \le \theta_{\mathbb{P}} \le 360°$.

With Eqns. (6) and (8), the characterized curves of the IWs of the S0 and A0 modes at 48 μs and 124 μs were obtained with $\mathbf{P}_{\text{CHC}}\{4, 0.5, 0°, 150\}$ and $\mathbf{P}_{\text{CHC}}\{4, 0.05, 0°, 150\}$ as shown in Figs. 6(a) and (b) respectively. The characterized curves (green-dots) illustrated that the curves were closely aligned with the wavefronts of S0 and A0 modes. Next, these parametric equations (Eqns. (6) and (8)) with the $\mathbf{P}_{\text{CHC}}$ of the characterized curves were saved and coded in LUIS for Process 2 to further quantify the similarity performance.

Hyperbolic Curve (HC)

The patterns of the reflected wavefronts differ from the pattern of the incident wavefronts. Figures 5(b)(c) and 6(c) show that the reflected wavefronts of the aluminum plate and the cross-ply CFRP plate were both similar to a hyperbolic curve, rather than a cyclic curve. The parametric equation of the hyperbolic curve is expressed below with the angle $\theta_{\mathbb{P}}$ ranging from –90° to 90°:

$$\breve{x} = \left(\frac{l\cos(\theta_{\mathbb{P}})}{1 - e\cos(\theta_{\mathbb{P}})} \right) + c \quad \text{and} \quad \breve{y} = \left(\frac{l\sin(\theta_{\mathbb{P}})}{1 - e\cos(\theta_{\mathbb{P}})} \right), \tag{9}$$

where, $\breve{x} \ge 0$, $a > 0$, and

$$l = \frac{b^2}{a}, \quad e = \sqrt{1 + \frac{b^2}{a^2}}, \quad \text{and} \quad c = \sqrt{a^2 + b^2}. \tag{10}$$

Figure 7(c) shows the hyperbolic plot on the $\mathbb{P}$-plane with the transverse axis ($\breve{x}$) and the conjugate axis ($\breve{y}$). The transverse axis is the chord or the line through the focus, and the conjugate axis is the line through the center perpendicular to the transverse axis. The a and b are the semi-major and semi-minor axes on the $\breve{x}$ and $\breve{y}$ axes respectively. In this plot (Fig. 7(c)), the a and b are set to 0.5 with the condition of $-90° < \theta_{\mathbb{P}} < 90°$. The l is known as the semilatus rectum, the e is the eccentricity of the hyperbola ($e > 1$), and the c is the distance of the focus from the center.

To match the size of the RWs in the $\mathbb{S}$-plane, the base hyperbolic curve $\breve{x} \ge 0$ in $\mathbb{P}$-plane as shown in Fig. 7(c) shall be considered first with the corresponding coordinates $(\breve{x}, \breve{y})$ generated from Eqn. (9) with the condition of $-90° < \theta_{\mathbb{P}} < 90°$. Then, in order to match the size of the desired RWs, the generated coordinates $(\breve{x}, \breve{y})$ are employed into the parametric equation of the characterized curve in $\mathbb{S}$-plane as expressed below:

$$\begin{bmatrix} x \\ y \end{bmatrix} = \hat{R}(\Omega) \begin{bmatrix} w_x \breve{x} + A_{\text{offset}} \\ w_y \breve{y} \end{bmatrix} \quad \text{and} \quad \hat{R}(\Omega) = \begin{bmatrix} \cos(\Omega) & -\sin(\Omega) \\ \sin(\Omega) & \cos(\Omega) \end{bmatrix}, \tag{11}$$

where $\hat{R}(\Omega)$ is the rotation matrix at the rotation angle (Ω), and A_{offset} is the offset distance of the concave of the characterized curve along the x-axis in $\mathbb{S}$-plane. The radius (R) of the center plate at the concave of the characterized curve is equaled to $aw_x + A_{\text{offset}}$ in $\mathbb{S}$-plane. In the expression, w_x and w_y are the half-length of the width and height of the plate respectively. Then, the characterized curve is generated with the conditions of $|x| \le w_x$ and $|y| \le w_y$. In this paper, the parameters and the scale factor of the characterized curve are grouped and denoted as $\mathbf{P}_{\text{H}}\{a, b, \Omega, A_{\text{offset}}\}$. With the coordinates (x, y) obtained from Eqn. (11), the corresponding polar coordinates $(\theta_{\mathbb{S}}, r_{\mathbb{S}})$ of the characterized curve in the $\mathbb{S}$-plane also can be obtained as well as expressed below:

$$\theta_{\mathbb{S}} = \tan^{-1}(y/x) \quad \text{and} \quad r_{\mathbb{S}} = \sqrt{x^2 + y^2}. \tag{12}$$

For the aluminum plate, using Eqns. (9) and (11), the characterized curves were obtained at the $\mathbf{P}_{\text{H}}\{0.5, 0.68, 90°, 0\}$ and $\mathbf{P}_{\text{H}}\{0.5, 1, 132°, 80\}$ for the RWs at the time instants of 88 μs (Fig. 5(b)) and 166 μs (Fig. 5(c)) respectively. Then, for the CFRP plate, the characterized curve was obtained at the $\mathbf{P}_{\text{H}}\{0.5, 0.35, 180°, 20\}$ for the RWs at the time instants of 84 μs (Fig. 6(c)). Lastly, the parameters and corresponding parametric equations (Eqns. (9)-(11)) of the characterized curves are saved and coded in LUIS to further quantify the similarity of the characterized curves of both plates.

3.3 Process 2 – Quantification of Parameterization

3.3.1 Incident Wavefront Characterization

Previously, the results of Process 1 were discussed, and the parametric equations of the characterized curves (circle, cyclic-harmonic curve, and hyperbolic curve) were determined and coded into the LUIS for Process 2. Next, this section will address the outcomes of Process 2.

Aluminum Plate

First, the coordinates (x, y) of the characterized curve was regenerated in LUIS based on the results obtained in Process 1. LUIS used these coordinates as an initial setting and performed the parametric curve scanning process to measure the ultrasonic signals. Hence, in aluminum plate case, the IWs of the S0 and A0 modes in the spatial ultrasonic wavefront image at the time instant of 45 μs (Fig. 5(a)) was considered in Process 2. Since the characterized curve was identified as a circle in Process 1, the LUIS performed the circle scan with the parametric curve equations (Eqns. (7) and (8)) at R = 170 mm to characterize the IWs of the S0 mode.

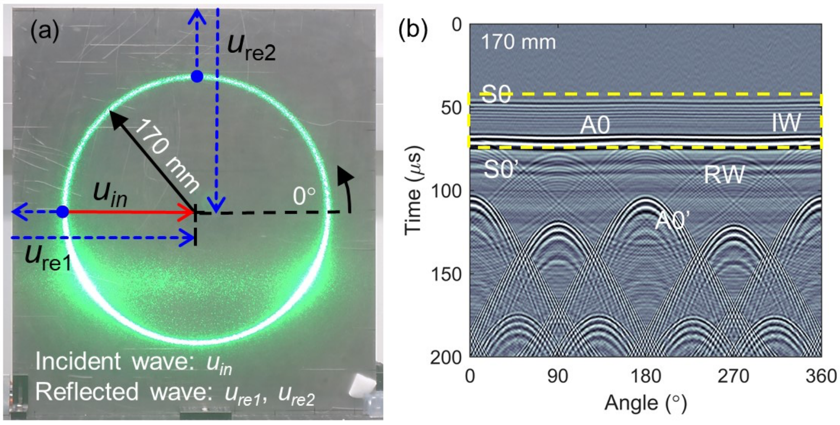

Figure 8. (a) Laser circle scanning pattern and (b) corresponding ultrasonic waves on the aluminum plate at R = 170 mm.

Figure 8(a) shows the laser circle scanning pattern on the aluminum plate at the radius of 170 mm. The circle coordinates (x, y) at R = 170 mm were generated based on Eqns. (7) and (8) in LUIS. With these coordinates, the LMS maneuvered the laser beam to impinge periodically at each scan point on the plate to generate local ultrasonic waves. The corresponding ultrasonic signals were measured with the in-line bandpass filter with the low-cutoff frequency of 50 kHz and the high-cutoff frequency of 500 kHz. The low shutter speed of the camera was set during the circle scanning process to provide enough time to capture a full circle scan as shown in Fig. 8(a). This camera setting was also configured to capture the other laser scanning curves in later part.

After the scanning process, the ultrasonic signals were measured and represented in PUWI with the angle-time domain as shown in Fig. 8(b). Ideally, if the wavefronts of the incident waves from all the directions are the same, these wavefronts should also travel at the same speed. Thus, the arrival time-deviation of the directions will be zero, and the same wavefronts will be displayed in PUWI in multiple straight lines along the angle-axis in PUWI. As shown in Fig. 8(b), the yellow-shaded box shows that all IWs arrived in the S0 mode at 45 μs and in A0 mode at 64 μs, and were shaped as the lines along the angle-axis.

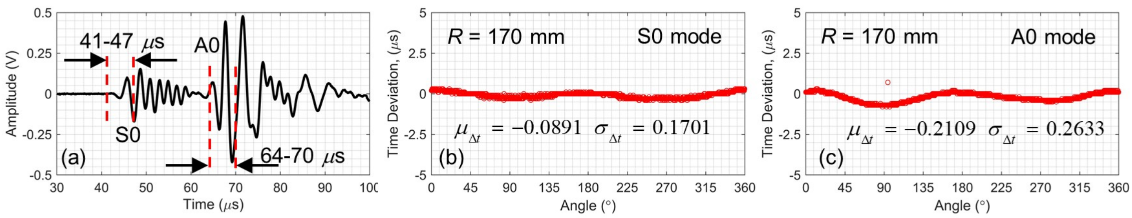

Figure 9. (a) Time history of reference ultrasonic signal ($u_{\mathrm{Ref}}(\theta_{\mathbb{S}}^{\mathrm{Ref}}, t)$) at $\theta_{\mathbb{S}}^{\mathrm{Ref}} = 180°$, arrival time-deviation of the ultrasonic responses ranging from 0° to 360° for (b) S0 mode and (c) A0 mode.

Based on Eqn. (3), the digitized reference ultrasonic signal $u_{\mathrm{Ref}}[m_{\mathrm{Ref}}, k]$ at the index $m_{\mathrm{Ref}} = 1068$ ($\theta_{\mathbb{S}}^{\mathrm{Ref}} = 180°$) was selected, as shown in Fig. 9(a), to calculate the arrival time-deviation for the IWs of the S0 and A0 modes. Figure 9(a) shows the time-history of the u_{Ref} from the PUWI in Fig. 8(b). To measure the arrival time-deviation Δt and mean arrival time-deviation $\mu_{\Delta t}$, the angle range and time window (t_W) were therefore set accordingly as tabulated in Table 1.

Table 1. Summary of angle range ($\Delta\theta_{\mathbb{S}}$) and time window ($t_W$) assigned to determine arrival time deviation (Δt) and mean arrival time-deviation ($\mu_{\Delta t}$) for IWs characterization in S0 and A0 modes.

Mode	$\Delta\theta_{\mathbb{S}}$ for Δt		Time Window, t_W		$\Delta\theta_{\mathbb{S}}$ for $\mu_{\Delta t}$	
	$\theta_{\mathbb{S}}^{\min}(m_{\min})$	$\theta_{\mathbb{S}}^{\max}(m_{\max})$	$t_{\min}(k_{\min})$	$t_{\max}(k_{\max})$	$\theta_{\mathbb{S}}^{\min}(m_{\min})$	$\theta_{\mathbb{S}}^{\max}(m_{\max})$
S0	0° (1)	360° (2136)	41 (205)	47 (235)	0° (1)	360° (2136)
A0	0° (1)	360° (2136)	64 (320)	70 (350)	0° (1)	360° (2136)

Figures 9(b) and (c) show that the arrival time-deviations for both S0 and A0 modes were approximated to the zero level. The $\mu_{\Delta t}$ of the S0 mode's IW was obtained at –0.0891 μs with the standard deviation $\sigma_{\Delta t}$ of 0.1701 μs; and the $\mu_{\Delta t}$ of the A0 Mode's IWs was obtained at -0.2109 μs with the standard deviation $\sigma_{\Delta t}$ of –0.2633 μs.

As an aside, in Fig. 8(b) it is noted that the RWs in 0°/360 and 180° directions traveled faster than the RWs (denoted as S0′) in 90° and 270° directions and interfered with the IWs of the A0 mode in the 64-70 μs time window. The difference in arrival times in the reflected waves is because they traveled in a rectangular aluminum plate that had different boundary lengths. It shows that the PUWI can be an alternative to UWI to analyze how reflected waves interact with the boundaries in the angle-time domain, which may be a useful feature to investigate the shape of a target in the NDE-SHM applications.

Since the ultrasonic wave at 180° was taken as the reference signal for Eqn. (3) to cross-correlate to the test signals, the magnitudes of the arrival time-deviations in the region approximately 90° and 270° are slightly higher than the other directions for the S0 and A0 modes (Figs. 9(b) and (c)), which has caused high values in the standard deviations of both cases. In A0 mode, however, the standard deviation is higher than the S0 mode. It is primarily attributable to the wavefronts of the reference signal (64 μs to 70 μs) at 180° for A0 mode, which has interfered with the reflected waves (S0′) and varies from the wavefronts of the A0 mode at about 90° and 270°.

In this isotropic case (aluminum plate), the characterization of the IWs for both modes is straightforward and only one parameter $\theta_{\mathbb{P}}$ and one scale factor R need to be considered. In addition, there is no need repetition of the scanning process with new updated parameters to improve the accuracy of the characterized curve. Subsequently, the laser circle scanning curve can easily characterize the IWs of the S0 and A0 modes with the condition where the sensor (S1) must be in the center of the circle. From a practical point of view, the contact sensor can be easily replaced with a non-contact sensor, such as the laser Doppler vibrometer (LDV) improve the implementation mobility.

CFRP Plate

In this subsection, the spatial ultrasonic wavefront characterization of the cross-ply CFRP plate was examined. The parametric CHC scan was performed to quantify the accuracy of the characterized curve with the parameters as predicted in Process 1. The CHC scanning process may be repeated with new updated parameter set to improve the accuracy of the characterized curve. The scanning process was then conducted further to verify the repeatability at various radii. The scanning process thus started in this paper with the radius (R) at first 150 mm, second at 80 mm, and third at 200 mm.

The experimental setup for the scanning process was configured like the case for the aluminum plate. The LUIS started the scanning process at the initial scanning point of $\theta_{\mathbb{S}} = 0°$ that was in parallel to the fiber direction 90° (yellow arrow in Fig. 10). Each ultrasonic signal with the total signal duration of 400 μs was then measured and sampled at 5 MHz. At the same $\mathbf{P}_{\mathrm{CHC}}$, the LUIS did the parametric scan twice to measure the ultrasonic signals in the in-line bandpass filter at two separate settings. The first measurement was set at the narrowband frequency of 140-160 kHz, and the second measurement at the broadband frequency of 50-500 kHz. The narrowband case and the broadband case are referred to as 140-160 kHz and 50-500 kHz respectively and are used in the rest of the discussion in this section. The total rounded scan points (L) of the complete scanned curve are expressed as $L = 2\pi R / \Delta S$, where ΔS is the interval arc-length between the two scan points. Hence, the L of 1885, 1005, and 2513 were obtained for the LUIS to conduct the scanning process in relation to the radius R of 150 mm, 80 mm, and 200 mm with the ΔS of 0.5 mm.

Since the IWs of the S0 and A0 modes in a cross-ply CFRP plate are typically symmetrical in the direction of the fiber (0° and 90°), the IWs in the angle ranges, from 90° to 180° and from 135° to

225°, were only considered in this paper to assess the accuracy of the characterized curve for the incident wavefronts. Tables 2 and 3 provide the summary of the variables settings in Eqns. (3) and (4) to calculate the arrival time-deviation accordingly. Then, two regions of the cross-ply CFRP plate, non-fiber direction region ($105° \le \phi_{\mathbb{S}} \le 165°$) and fiber direction region ($165° \le \phi_{\mathbb{S}} \le 195°$), were preliminary assigned in this paper to determine the mean arrival time-deviation via Eqn. (5). Authors are aware that there may be variations in the angle ranges of both directions as per the cross-ply CFRP plate being made.

Table 2. Summary of angle range $90° \le \theta_{\mathbb{S}} \le 180°$ and time window set to determine arrival time-deviation (Δt) at various radius R for IW characterization in S0 and A0 modes. (*Narrowband case and **Broadband case)

R (mm)	Angle Range		Time Window, t_W			
	$\theta_{\mathbb{S}}^{\min} = 90°$	$\theta_{\mathbb{S}}^{\max} = 180°$	S0 Mode		A0 Mode	
	$m_{\min}$	$m_{\max}$	$t_{\min}(k_{\min})$	$t_{\max}(k_{\max})$	$t_{\min}(k_{\min})$	$t_{\max}(k_{\max})$
150	471	943	45(225)*	60(300)*	130(650)*	145(725)*
			45(225)**	60(300)**	125(625)**	140(700)**
80	251	503	32(160)*	55(275)*	80(400)*	95(475)*
			32(160)**	45(225)**	75(375)**	90(450)**
200	628	1257	52(260)*	70(350)*	160(800)*	175(875)*
			52(260)**	70(350)**	150(750)**	165(825)**

Table 3. Summary of angle range $135° \le \theta_{\mathbb{S}} \le 225°$ and time window set to determine arrival time-deviation (Δt) at various radius R for the IW characterization in S0 and A0 modes. (*Narrowband case and **Broadband case)

R (mm)	Angle Range		Time Window, t_W			
	$\theta_{\mathbb{S}}^{\min} = 135°$	$\theta_{\mathbb{S}}^{\max} = 225°$	S0 Mode		A0 Mode	
	$m_{\min}$	$m_{\max}$	$t_{\min}(k_{\min})$	$t_{\max}(k_{\max})$	$t_{\min}(k_{\min})$	$t_{\max}(k_{\max})$
150	706	1177	45(225)*	65(325)*	125(625)*	140(700)*
			40(200)**	55(275)**	120(600)**	135(675)**
80	377	628	33(165)*	55(275)*	80(400)*	95(475)*
			30(150)**	45(225)**	70(350)**	85(425)**
200	942	1571	50(250)*	70(350)*	163(815)*	178(890)*
			50(250)**	65(325)**	150(750)**	165(825)**

The LUIS conducted the parametric CHC scanning at the initial scanning process according to the $\mathbf{P}_{\text{CHC}}\{4, 0.05, 0°, 150\}$ and $\mathbf{P}_{\text{CHC}}\{4, 0.5, 0°, 150\}$ of the characterized curves obtained from the Process 1 to characterize the IWs of S0 mode in non-fiber and fiber direction regions, respectively. The scanning process was then repeated with a new updated $\mathbf{P}_{\text{CHC}}$ until the $\mu_{\Delta t}$ reach a minimum value (ideally, zero). Hence, the lower the mean arrival time-deviation $\mu_{\Delta t}$, the more precise the characterized curve to the desired spatial wavefront pattern is. As mentioned earlier in section 2, the updating process on the $\mathbf{P}_{\text{CHC}}$ was done manually. Finally, the updated $\mathbf{P}_{\text{CHC}}\{4, 0.085, 0°, 150\}$ and $\mathbf{P}_{\text{CHC}}\{4, 0.8, -2°, 150\}$ were acquired to characterize the IWs of the S0 mode in non-fiber and fiber direction regions respectively, and the corresponding patterns of the laser scanning curve were captured as shown in Figs. 10(a) and (b).

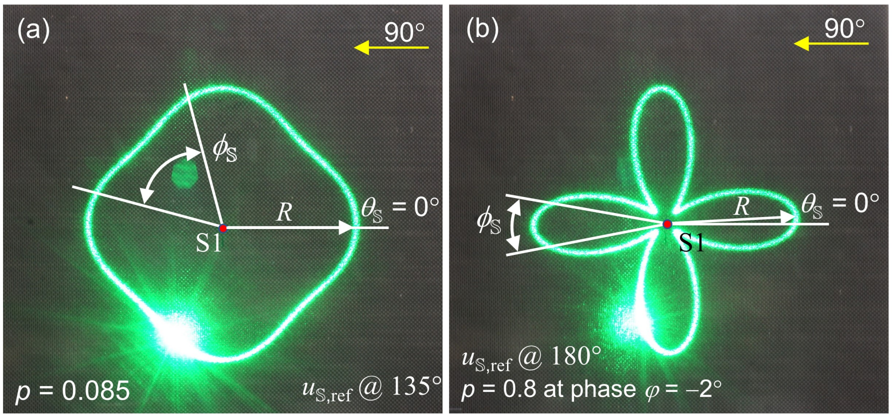

Figure 10. Cyclic-harmonic scanning curves on cross-ply CFRP plate at updated parameters (a) $\mathbf{P}_{\text{CHC}}\{4, 0.085, 0°, 150\}$ and (b) $\mathbf{P}_{\text{CHC}}\{4, 0.8, -2°, 150\}$ for IWs of S0 mode in non-fiber and fiber direction regions respectively.

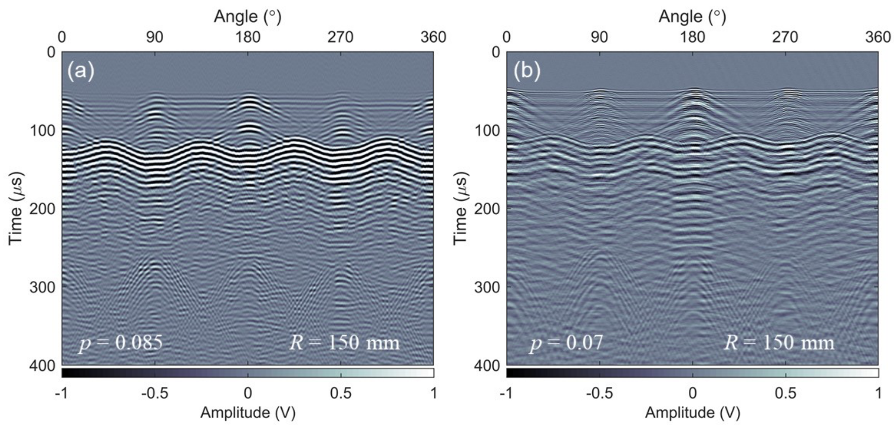

Figure 11. Ultrasonic responses in non-fiber direction region with (a) 140-160 kHz and (b) 50-500 kHz based on cyclic-harmonic scanning curves at $\mathbf{P}_{\text{CHC}}\{4, 0.085, 0°, 150\}$ and $\mathbf{P}_{\text{CHC}}\{4, 0.07, 0°, 150\}$ respectively.

Figures 11(a) and (b) show the corresponding measured ultrasounds in the non-fiber direction region with the narrowband frequency and broadband frequency at $\mathbf{P}_{\mathrm{CHC}}\{4, 0.085, 0°, 150\}$ and $\mathbf{P}_{\mathrm{CHC}}\{4, 0.07, -2°, 150\}$, respectively. Figure 12(a) displays the zoomed PUWI of the ultrasonic responses from 90° to 180° in Fig. 11(a) with the time window from 40 μs to 100 μs. By observing the zoomed PUWI, the IWs of the SH0 mode (as indicated in the red ellipses) surface about 105° to 165° in the non-fiber direction region. This also indicates that the waves of the S0 mode were starting to separate from the SH0 mode since the S0 mode has higher wave speed than the SH0 mode. Then, the IWs in the fiber direction region were dominated by the S0 mode. Based on Eqns. (3) and (4) with the settings in Table 2, the respective arrival time-deviations with the reference signal u_{Ref} at 135° ($m_{\mathrm{Ref}} = 706$) were determined as shown in Fig. 12(d). The mean arrival time-deviation was then determined by Eqn. (5) and the results were tabulated in Table 4.

In the case of narrowband inputs, the characterized IWs of the S0 mode at the $\mathbf{P}_{\mathrm{CHC}}\{4, 0.085, 0°, 150\}$ were obtained with the $\mu_{\Delta t} = -0.0229$ μs and the standard deviation $\sigma_{\Delta t}$ of 0.1854 μs. It shows that the laser CHC scan at $\mathbf{P}_{\mathrm{CHC}}\{4, 0.085, 0°, 150\}$ is capable of characterizing the same wavefronts of S0 mode in non-fiber direction region with only the maximum absolute deviation (MAD), expressed as $\arg\max\{|\mu_{\Delta t} \pm \sigma_{\Delta t}|\}$, of 0.2083 μs as equivalent to just one sample time (T_{S}) of the measurement used in the experiment. In contrast, the arrival time-deviations determined in the direction ranges of $90° < \theta_{\mathbb{S}} < 105°$ and $165° < \theta_{\mathbb{S}} < 180°$ were dispersed away from the zero level. Therefore, the laser CHC scan at $\mathbf{P}_{\mathrm{CHC}}\{4, 0.085, 0°, 150\}$ demonstrated better ability to characterize the same IWs of the S0 mode in the non-fiber direction region with $105° \le \phi_{\mathbb{S}} \le 165°$ compared to fiber-direction region.

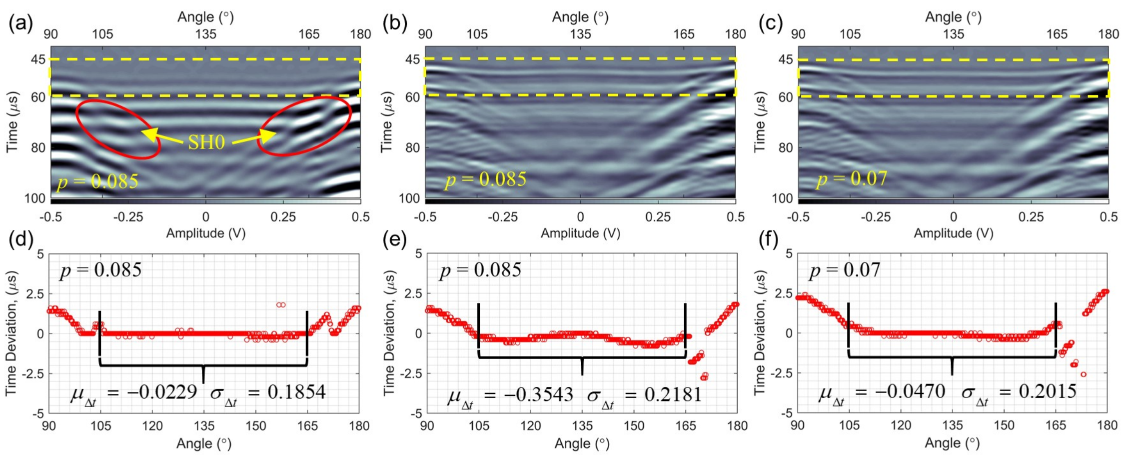

Figure 12. Ultrasonic responses with frequency bands of (a) 140-160 kHz and (b)(c) 50-500 kHz ranging from 90° to 180°, and corresponding arrival time-deviations (d) and (e)(f) respectively, based on the laser CHC scan at $\mathbf{P}_{\text{CHC}}\{4, 0.085, 0°, 150\}$ and $\mathbf{P}_{\text{CHC}}\{4, 0.07, 0°, 150\}$.

Table 4. Summary of mean arrival time-deviation for IW characterization in S0 mode using laser CHC scanning method with narrowband of 140 kHz-160 kHz.

$\mathbf{P}_{\text{CHC}}\{n, p, \varphi, R\}$	Non-fiber direction region		Fiber direction region		MAD (μs)
	$\mu_{\Delta t}$	$\sigma_{\Delta t}$	$\mu_{\Delta t}$	$\sigma_{\Delta t}$	
{4, 0.085, 0°, 150}	–0.0229	0.1854	-	-	0.2083
{4, 0.085, 0°, 80}	–0.0012	0.3522	-	-	0.3534
{4, 0.07, 0°, 200}	–0.0076	0.1467	-	-	0.1543
{4, 0.8, –2°, 150}	-	-	–0.0174	0.7256	0.7430
{4, 0.8, –2°, 80}	-	-	–0.0476	0.6480	0.6956
{4, 0.8, –2°, 200}	-	-	–0.3286	0.9135	1.2421

In the case of broadband, the same $\mathbf{P}_{\text{CHC}}\{4, 0.085, 0°, 150\}$ was first used to characterize the IWs of the S0 mode as shown in Fig. 12(b). The corresponding arrival time-deviation was determined as shown in Fig. 12(e) with the $\mu_{\Delta t}$ of –0.3543 μs and the $\sigma_{\Delta t}$ of 0.2181 μs. It reveals that the laser CHC scanning at $\mathbf{P}_{\text{CHC}}\{4, 0.085, 0°, 150\}$ was less accurate in the broadband case (50-500 kHz) as compared to the narrowband case. Therefore, the scanning process was reiterated and halted at the new updated parameters $\mathbf{P}_{\text{CHC}}\{4, 0.07, 0°, 150\}$ (Fig. 10(b)), and the corresponding ultrasounds were measured as shown in Fig. 11(b). Figures 12(c) and (f) show the zoomed PUWI of Fig. 11(b) and the corresponding arrival time-deviation, respectively.

At this new updated $\mathbf{P}_{\text{CHC}}\{4, 0.07, 0°, 150\}$, the accuracy of the arrival time-deviation measurement was improved with $\mu_{\Delta t} = -0.047\,\mu\text{s}$ and $\sigma_{\Delta t} = 0.2015\,\mu\text{s}$ (as tabulated in Table 5), compared to previous results at $\mathbf{P}_{\text{CHC}}\{4, 0.085, 0°, 150\}$ (Fig. 12(e)). This shows that the measurement of the same IWs of the S0 mode in the broadband case (50-500 kHz) was improved by a minor adjustment the parameter of p = 0.085 to p = 0.07. The MAD was determined at 0.2485 μs (Table 5) and showed small difference to the MAD of the narrowband case (Table 4).

Table 5. Summary of mean arrival time-deviation for IW characterization in S0 mode using laser CHC scanning method with broadband of 50 kHz-500 kHz.

$\mathbf{P}_{\mathrm{CHC}}\{n, p, \varphi, R\}$	Non-fiber direction region		Fiber direction region		MAD (μs)
	$\mu_{\Delta t}$	$\sigma_{\Delta t}$	$\mu_{\Delta t}$	$\sigma_{\Delta t}$	
{4, 0.07, 0°, 150}	–0.0470	0.2015	-	-	0.2485
{4, 0.07, 0°, 80}	–0.3148	0.3877	-	-	0.7025
{4, 0.07, 0°, 200}	–0.1919	0.2761	-	-	0.4680
{4, 0.8, –2°, 150}	-	-	–0.1165	0.9602	1.0767
{4, 0.8, –2°, 80}	-	-	–0.0738	0.9718	1.0456
{4, 0.8, –2°, 200}	-	-	–0.1905	1.1083	1.2988

The laser CHC scan showed the positive ability not only to characterize the IWs of the S0 mode with the narrowband frequency but also with the broadband frequency in the non-fiber direction region $105° \le \phi_{\mathbb{S}} \le 165°$. However, as shown in Figs. 12(d) and (f), in the fiber direction regions $90° \le \theta_{\mathbb{S}} < 105°$ and $165° < \theta_{\mathbb{S}} \le 180°$, both $\mathbf{P}_{\mathrm{CHC}}$ were unable to characterize the IWs of the S0 mode. Regarding this, in this paper, another parametric scanning curve was considered to characterize the IWs of the S0 mode in fiber direction region $165° \le \phi_{\mathbb{S}} \le 195°$. By referring to the spatial ultrasonic wavefront image in Fig. 6(a), the LUIS carried out the CHC scanning curve on the initial parameters $\mathbf{P}_{\mathrm{CHC}}\{4, 0.5, 0°, 150\}$ of the characterized curve obtained in Process 1 and the updating process stopped at the new $\mathbf{P}_{\mathrm{CHC}}\{4, 0.8, -2°, 150\}$.

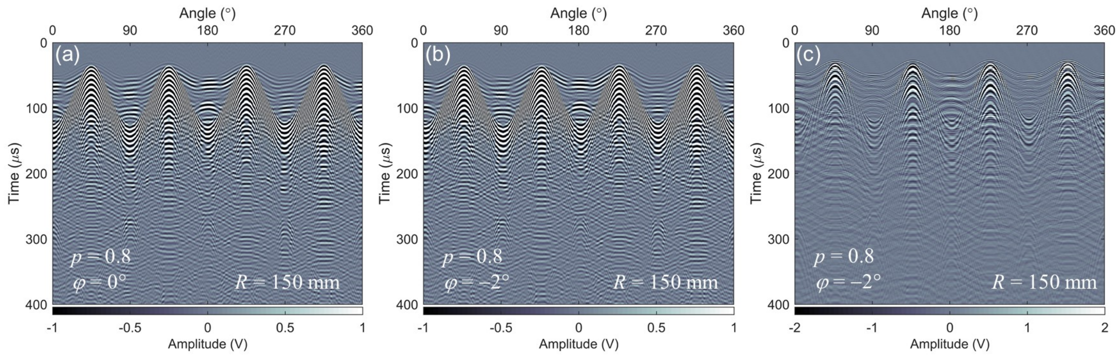

Figure 13. Ultrasonic responses with the frequency bands of (a)(b) 140-160 kHz and (c) 50-500 kHz based on cyclic-harmonic scanning curves at (a) $\mathbf{P}_{\mathrm{CHC}}\{4, 0.8, 0°, 150\}$ and (b)(c) $\mathbf{P}_{\mathrm{CHC}}\{4, 0.8, -2°, 150\}$ respectively.

Before the measured ultrasound at $\mathbf{P}_{\mathrm{CHC}}\{4, 0.8, -2°, 150\}$ is examined, it is important to discuss the measured ultrasound at $\mathbf{P}_{\mathrm{CHC}}\{4, 0.8, 0°, 150\}$ as shown in Figs. 13(a) and 14(a). Figure 14(a) shows the enlarged Fig. 13(a) ranging from 135° to 225°. The patterns of the measured wavefronts in the fiber direction region were different, compared to previous case in the non-fiber direction region at $\mathbf{P}_{\mathrm{CHC}}\{4, 0.085, 0°, 150\}$ (Fig. 11). Looking at Fig. 14(a), the IWs of the S0 mode did not arrive at the same time in the fiber direction region ($165° \leq \phi_{\mathbb{S}} \leq 195°$). In fact, the arrival time of the same IWs was gradually shorter starting from 165° to 195° and the arrival time-deviations formed a titled line with a slanted angle. This result could imply that there were fiber stacking variations in this local region during the manufacture of the CFRP plate. For this, the $\mathbf{P}_{\mathrm{CHC}}\{4, 0.8, 0°, 150\}$ was updated to $\mathbf{P}_{\mathrm{CHC}}\{4, 0.8, -2°, 150\}$ by altering the phase φ from 0° to −2° to Eqn. (6), and the rotated laser CHC scanning curve by −2° is shown in Fig. 10(b).

Figure 13(b) shows the corresponding PUWI (narrowband) ranging from 0° to 360° at the updated $\mathbf{P}_{\mathrm{CHC}}\{4, 0.8, -2°, 150\}$, and the zoomed version, ranging from 135° to 225°, is plotted as shown in Fig. 14(b). By comparing the wavefronts in Figs. 14(a) and (b), it illustrates that the rotated CHC at φ = −2° was able to capture the IWs of the S0 mode arrive at the same arrival time. In the case of broadband, the $\mathbf{P}_{\mathrm{CHC}}\{4, 0.8, -2°, 150\}$ was also used in the LUIS for the measurement and the corresponding PUWI is plotted as shown in Figs. 13(c) and 14(c).

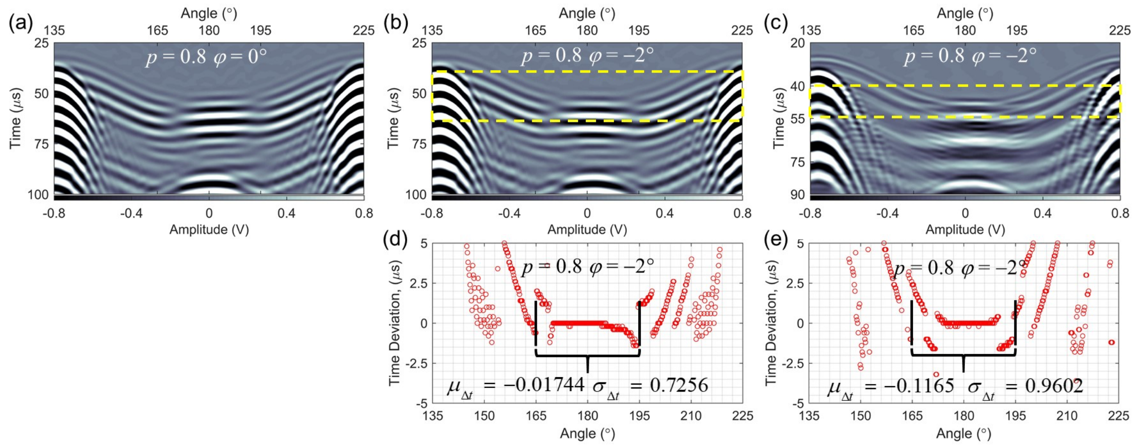

Figure 14. Ultrasonic responses in narrowband case based on laser cyclic-harmonic curve scan at (a) $\mathbf{P}_{\mathrm{CHC}}\{4, 0.8, 0°, 150\}$ and (b) $\mathbf{P}_{\mathrm{CHC}}\{4, 0.8, -2°, 150\}$. (c) Ultrasonic responses in broadband case. (d)(e) Arrival time-deviations of narrowband and broadband respectively.

For the narrowband and broadband cases, respectively, the u_{Ref} at 180° ($m_{\mathrm{Ref}} = 942$) was selected to assess the arrival time-deviations with the angle range and time window settings as tabulated in Table 3. Figures 14(d) and (e) indicate the arrival time-deviations for the cases of narrowband and broadband, respectively. Both cases show that the values of the arrival time-deviations in the fiber direction region (165° to 195°) were approximately zero. The arrival time-deviations between 165° and 195° as shown in Figs. 14(d) and (e) were then introduced into Eqn. (5) to calculate the mean arrival time-deviations. Tables 4 and 5 indicate the results of the mean arrival time-deviation for the cases of narrowband and broadband, respectively.

In the narrowband case, the $\mu_{\Delta t}$ was determined to be –0.01744 μs with a $\sigma_{\Delta t}$ of 0.7256 μs. Then, in the broadband case, the $\mu_{\Delta t}$ was determined to be –0.1165 μs with a $\sigma_{\Delta t}$ at 0.9602 μs. The MAD in Tables 4 and 5 also shows that the narrowband case (0.7430 μs) has better estimate than the broadband case (1.0767 μs). But, both MADs in the case of fiber direction region are higher than the case of non-fiber region. As a result, the characterization of IWs of S0 mode in the case of fiber direction region is less accurate compared to the case of non-fiber region.

Even though $\mu_{\Delta t}$ was close to zero in the fiber direction region, the corresponding $\sigma_{\Delta t}$ is high in the cases of narrowband and broadband. The high standard deviations are primarily due to the incorrect estimate of the arrival time-deviations from 165° to 169.5° and from 185.5° to 195° for the narrowband case, and from 165° to 174° and from 189° to 195° for the broadband case. These incorrect estimates are due to the separation of the S0 and SH0 modes at these directions, as shown in Figs. 14(b) and (c). Thus, for the cases of narrowband and broadband, respectively, the laser CHC scan with the $\mathbf{P}_{\text{CHC}}\{4, 0.8, -2°, 150\}$ demonstrates the ability to characterize the IWs of the S0 mode in the fiber direction region ranging only from 169.5° to 185.5° and 174° to 189° in this paper. It reveals that the parameter $\mathbf{P}_{\text{CHC}}\{4, 0.8, -2°, 150\}$ is able to characterize the S0 mode in the fiber direction region with the angular range of about 16° and 15° for the narrowband and broadband cases respectively. It is noted that the angular range can vary as may depend upon the nature of the specimen being manufactured.

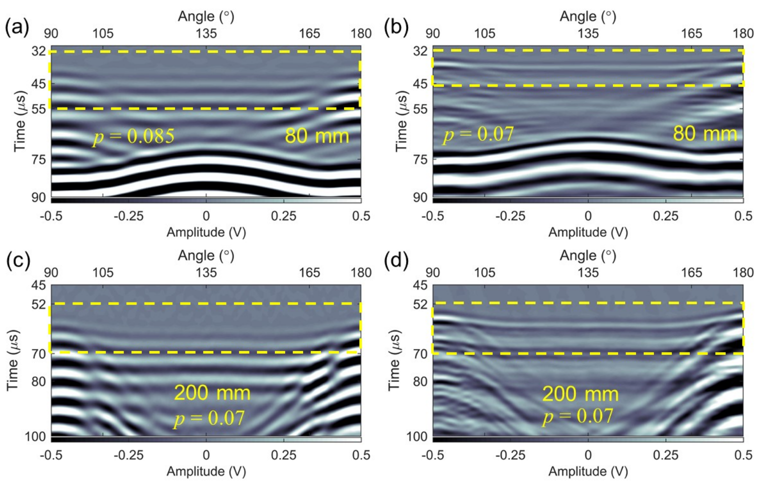

Figure 15. Ultrasonic responses with frequency bands of (a)(c) 140-160 kHz and (b)(d) 50-500 kHz ranging from 90° to 180° at the cyclic-harmonic scanning curves at (a) $\mathbf{P}_{\text{CHC}}\{4, 0.085, 0°, 80\}$, (b) $\mathbf{P}_{\text{CHC}}\{4, 0.07, 0°, 80\}$, and (c)(d) $\mathbf{P}_{\text{CHC}}\{4, 0.07, 0°, 200\}$.

Next, in order to further check the accuracy of the parameters against the change in radius, the same elements of $\mathbf{P}_{\text{CHC}}\{4, 0.085, 0°, R\}$ obtained in the non-fiber direction region (Fig. 12) were tested at the different radius *R* (80 mm and 200 mm). Hence, the LUIS initially performed the CHC scanning processes with the modified parameters $\mathbf{P}_{\text{CHC}}\{4, 0.085, 0°, 80\}$ and $\mathbf{P}_{\text{CHC}}\{4, 0.085, 0°, 200\}$ with the same experimental setup of 150 mm. Noted that the $\mathbf{P}_{\text{CHC}}$ elements were remained the same, but the *R* was changed to 80 mm and 200 mm for the narrowband and broadband cases, respectively. In the narrowband case, after the updating process for *R* = 80 mm, the $\mathbf{P}_{\text{CHC}}$ remained unchanged at $\mathbf{P}_{\text{CHC}}\{4, 0.085, 0°, 80\}$, but in the broadband case, the $\mathbf{P}_{\text{CHC}}$ was updated to $\mathbf{P}_{\text{CHC}}\{4, 0.07, 0°, 80\}$. Then, for *R* = 200 mm, the $\mathbf{P}_{\text{CHC}}$ was updated to $\mathbf{P}_{\text{CHC}}\{4, 0.07, 0°, 200\}$ for both narrowband and broadband cases.

Figures 15(a) and (b) show the measured IWs of the S0 mode at 80 mm for the narrowband and broadband frequencies, respectively. With the reference signal u_{Ref} at 135° ($m_{\text{Ref}} = 377$) and the angle range and time windows as tabulated in Table 2, the corresponding arrival time-deviations of the IWs were determined. Then, the mean arrival time-deviations from 105° to 165° were determined and tabulated in Tables 4 and 5.

In the narrowband case, the $\mu_{\Delta t}$ was obtained to be –0.0012 μs with a $\sigma_{\Delta t}$ of 0.3522 μs. It shows that the $\mathbf{P}_{\text{CHC}}\{4, 0.05, 0°, 80\}$ was able to measure the same IWs of the S0 mode from 105° to 165° in the non-fiber direction region. In the broadband case, the $\mu_{\Delta t}$ was found to be –0.3148 μs with a $\sigma_{\Delta t}$ of 0.3877 μs. Both standard deviations are almost the same and are attributed to the wrong measurement in 105° to 110° and 159° to 165°. It is found that the $\mu_{\Delta t}$ was obtained to be –0.3148 μs in the case of broadband that is substantially different from the $\mu_{\Delta t}$ in the case of narrowband at –0.0012 μs. Since both standard deviations are about the same (Tables 4 and 5), the high $\mu_{\Delta t}$ obtained in the broadband case is due to the fact that the selected reference signal at 135° traveled faster than the test signals in the non-fiber direction region. As the result, the MAD is obtained by an additional 98.9% at 0.7025 μs and higher than the narrowband case.

Figures 15(c) and (d) show the measured IWs of the S0 mode at 200 mm for the narrowband and broadband frequencies, respectively. The corresponding arrival time-deviations of the IWs were determined with the reference signal u_{Ref} at 135° ($m_{\text{Ref}} = 943$) and the angle range and time windows as shown in Table 2. The mean arrival time-deviations from 105° to 165° were then calculated and tabulated in Tables 4 and 5.

In the case of the narrowband input, the $\mu_{\Delta t}$ was determined to be –0.0076 μs with a $\sigma_{\Delta t}$ at –0.1467 μs, and in the case of broadband, the $\mu_{\Delta t}$ was determined to be –0.1919 μs with a $\sigma_{\Delta t}$ at 0.2761 μs. The MADs were obtained at 0.1543 μs and 0.4680 μs for the narrowband and broadband cases, respectively. Based on MAD in Tables 4 and 5, in all three separate radii, the narrowband case demonstrated better characterization of the S0 mode IWs as compared to the broadband case.

Next, the IWs of the S0 mode at the radii of 80 mm and 200 mm were considered in the fiber direction region. Both cases in the narrowband and broadband frequencies were used the same elements of the parameter (n = 4, p = 0.8, φ = –2°) as employed in previous 150 mm case. The experimental setup for the cases of 80 mm and 200 mm was same to the case of 150 mm except that the radius in LUIS was altered accordingly.

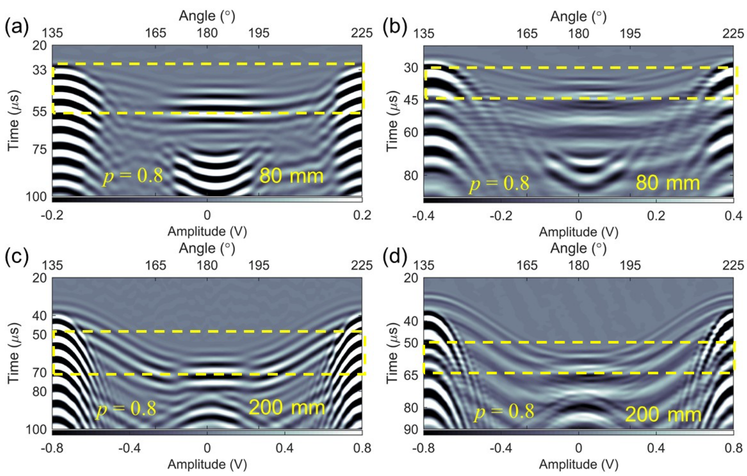

Figure 16. Ultrasonic responses with frequency bands of (a)(c) 140-160 kHz and (b)(d) 50-500 kHz ranging from 135° to 225° based on the cyclic-harmonic scanning curves at (a)(b) $\mathbf{P}_{\text{CHC}}\{4, 0.8, -2°, 80\}$ and (c)(d) $\mathbf{P}_{\text{CHC}}\{4, 0.8, -2°, 200\}$.

Figures 16(a) and (b) show the measured IWs of the S0 mode at the $\mathbf{P}_{\text{CHC}}\{4, 0.8, -2°, 80\}$ for the cases of narrowband and broadband respectively. With the reference signal u_{Ref} at 180° ($m_{\text{Ref}} = 503$), the corresponding arrival time-deviations of the IWs were determined according to the angle range and the time window as tabulated in Table 3. The mean arrival time-deviations were then calculated and tabulated in Tables 4 and 5. The $\mu_{\Delta t}$ was obtained as –0.0476 μs with a $\sigma_{\Delta t}$ of –0.6480 μs in the case of narrowband and –0.0738 μs with a $\sigma_{\Delta t}$ of –0.9718 μs in the case of broadband. The corresponding MADs were determined at 0.6956 μs and 1.0456 μs for the cases of narrowband and broadband respectively.

Figures 16(c) and (d) show the measured IWs of the S0 mode at the radius of 200 mm with the narrowband and broadband frequencies respectively at the $\mathbf{P}_{\mathrm{CHC}}\{4, 0.8, -2°, 200\}$. The corresponding arrival time-deviations of the IWs were determined with the reference signal u_{Ref} at 180° ($m_{\mathrm{Ref}} = 1257$), the angle range and the time windows as tabulated in Table 3 for both narrowband and broadband cases respectively. Then, the mean arrival time-deviations were determined and tabulated in Tables 4 and 5. The $\mu_{\Delta t}$ for both frequency bands were obtained to be –0.3286 μs and –0.1905 μs and the standard deviations are –0.9135 μs and –1.1083 μs, respectively. The corresponding MADs were determined at 1.2421 μs and 1.2988 μs.

Table 4 shows that the updated $\mathbf{P}_{\mathrm{CHC}}$ has a better characterization of the S0 mode IWs in the narrowband frequency compared to the broadband frequency (Table 5), especially in non-fiber direction region. The laser CHC scanning method also shows the ability to characterize the IWs of the S0 mode even at different radius. In addition, the accuracy of the characterization presented in Tables 4 and 5 demonstrated that it is highly dependent upon the selected reference signal. The results also show that the laser CHC scan was sensitive to the quality of the wavefronts. If the wavefronts are contaminated due to mode separation (Fig. 12) or change in localized properties (Fig. 14(a)), the arrival time-deviations would be incorrectly obtained. Although the proposed method is sensitive to the conditions of the IWs, it is also beneficial as a guide to show the location of the contaminated wavefronts where it is possible to avoid the placement of the sensor. Based on the parameters obtained for S0 mode in the above studies, the proposed method was able to characterize the spatial wavefront with the promising results based on the mean arrival time-deviation and MAD.

Next, the proposed method is further test on the spatial wavefronts of the A0 mode. The incident wavefront of the A0 mode in the non-fiber direction region was considered and followed by the incident wavefront of the A0 mode in fiber direction region. These two were also tested for the narrowband and broadband cases at radii 150 mm, 80 mm, and 200 mm. The experimental configurations were not changed and remained the same as performed in the previous case of the S0 mode.

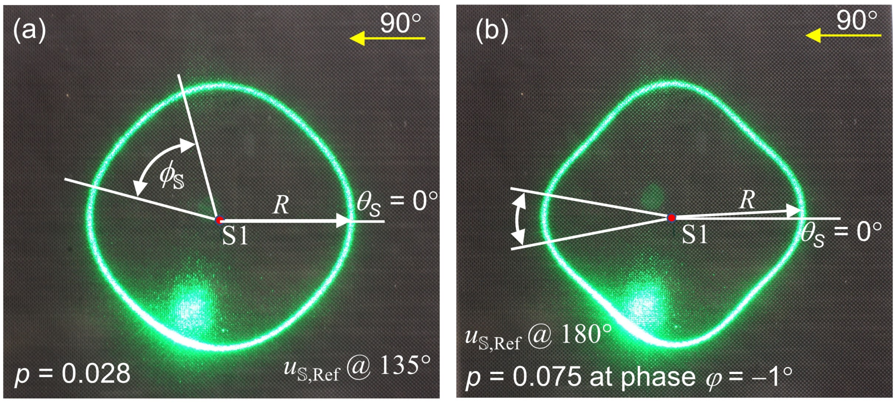

Figure 17. Cyclic-harmonic scanning curves on cross-ply CFRP plate at updated parameters (a) $\mathbf{P}_{\text{CHC}}\{4, 0.028, 0°, 150\}$ and (b) $\mathbf{P}_{\text{CHC}}\{4, 0.07, -1°, 150\}$ for IWs of A0 mode.

Based on Fig. 6(b) in Process 1, the characterized curve with the $\mathbf{P}_{\text{CHC}}\{4, 0.05, 0°, 150\}$ was used as the initial settings for the LUIS to perform the laser CHC scan to measure the ultrasonic signals. The LUIS repeated the scanning process and then it stopped at the updated parameter $\mathbf{P}_{\text{CHC}}\{4, 0.028, 0°, 150\}$ with low mean arrival time-deviation as desired to characterize the IWs of the A0 mode in the non-fiber direction region (105° to 165°). Figure 17(a) shows the corresponding laser cyclic-harmonic scanning curves at the updated parameter $\mathbf{P}_{\text{CHC}}\{4, 0.028, 0°, 150\}$.

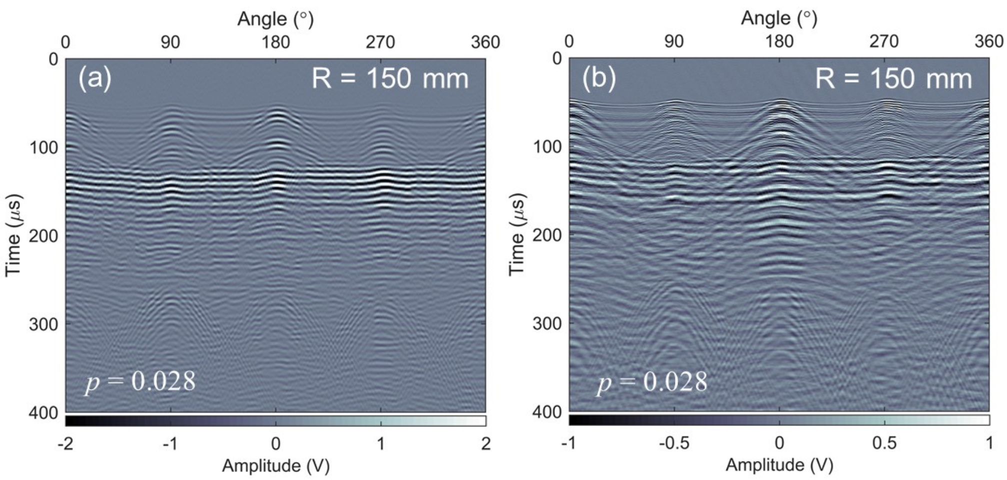

Figure 18. Ultrasonic responses with (a) 140-160 kHz and (b) 50-500 kHz based on the cyclic-harmonic scanning curves at $\mathbf{P}_{\text{CHC}}\{4, 0.028, 0°, 150\}$.

Figures 18(a) and (b) show the PUWI at the updated $\mathbf{P}_{\text{CHC}}\{4, 0.028, 0°, 150\}$, and Figs. 19(a) and (b) show the zoomed PUWI of Figs. 18(a) and (b), respectively. Based on Eqns. (3) and (4), for the narrowband and broadband cases, the arrival time-deviations were determined with the reference signal u_{Ref} at 135° ($m_{\text{Ref}} = 706$), the angle range, and the time windows as tabulated in Table 2. Then, the mean arrival time-deviations in the non-fiber direction region were determined via Eqn. (5) and the results were tabulated in Tables 6 and 7 for both cases.

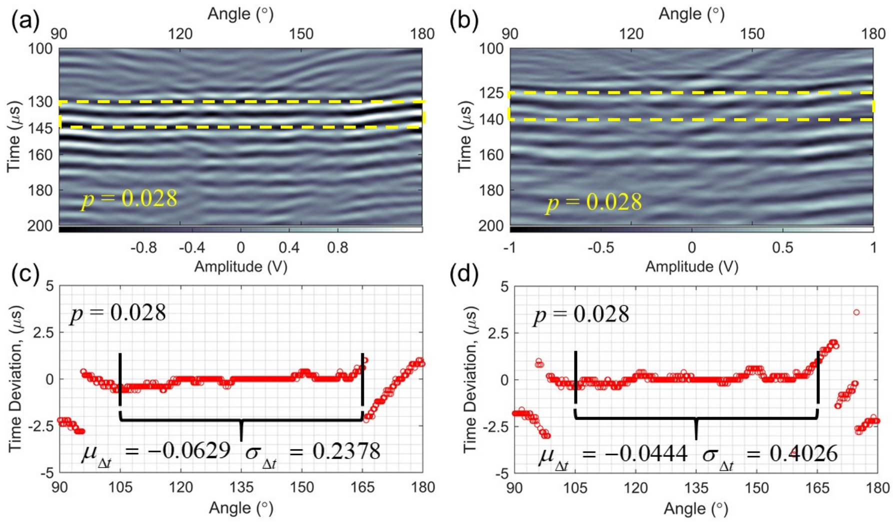

Figure 19. Ultrasonic responses with frequency bands of (a) 140-160 kHz and (b) 50-500 kHz ranging from 90° to 180°, and (c)(d) corresponding arrival time-deviations respectively, based on the cyclic-harmonic scanning curves at $\mathbf{P}_{\text{CHC}}\{4, 0.028, 0°, 150\}$.

Figure 19(c) shows that the $\mu_{\Delta t}$ was obtained to be –0.0629 μs with a $\sigma_{\Delta t}$ of 0.2378 μs in the case of narrowband. Although the IWs of the A0 mode at 150 mm were more contaminated than the IWs of the S0 mode (Fig. 12), the parameter $\mathbf{P}_{\text{CHC}}\{4, 0.028, 0°, 150\}$ was still capable to characterizing the IWs of the A0 mode in the non-fiber direction region. On the other hand, the arrival time-deviation began to deviate from the non-fiber direction region to the fiber direction region and it demonstrates that the $\mathbf{P}_{\text{CHC}}\{4, 0.028, 0°, 150\}$ was unable to characterize the IWs of the A0 mode in the fiber direction region.

In the broadband case (Fig. 19(d)), the $\mu_{\Delta t}$ was found to be –0.0444 μs with a $\sigma_{\Delta t}$ of 0.4026 μs as shown in Table 7. The arrival time-deviation shows similar scenarios to the narrowband case, which deviated from the non-fiber direction region to the fiber direction region. The standard deviation in the broadband case is higher than the narrowband case. This may be due to the dispersive waves travelling at various wave speeds where the wave speed of the selected reference signal u_{Ref} may be different from the signals of other propagation directions.

Table 6. Summary of mean arrival time-deviation for IW characterization in A0 mode using laser CHC scanning method with narrowband of 140 kHz-160 kHz.

$\mathbf{P}_{\mathrm{CHC}}\{n, p, \varphi, R\}$	Non-fiber direction region		Fiber direction region		MAD (µs)
	$\mu_{\Delta t}$	$\sigma_{\Delta t}$	$\mu_{\Delta t}$	$\sigma_{\Delta t}$	
{4, 0.028, 0°, 150}	–0.0629	0.2378	-	-	0.3007
{4, 0.028, 0°, 80}	–0.0308	0.1732	-	-	0.2040
{4, 0.026, 0°, 200}	–0.1338	0.4058	-	-	0.5396
{4, 0.075, –1°, 150}	-	-	–0.0278	0.2075	0.2353
{4, 0.075, –1°, 80}	-	-	–0.0376	0.2059	0.2435
{4, 0.075, –1°, 200}	-	-	–0.3377	0.3769	0.7146

Table 7. Summary of mean arrival time-deviation for IWs of A0 mode characterization using laser CHC scanning method with broadband of 50 kHz-500 kHz.

$\mathbf{P}_{\mathrm{CHC}}\{n, p, \varphi, R\}$	Non-fiber direction region		Fiber direction region		MAD (µs)
	$\mu_{\Delta t}$	$\sigma_{\Delta t}$	$\mu_{\Delta t}$	$\sigma_{\Delta t}$	
{4, 0.028, 0°, 150}	–0.0444	0.4026	-	-	0.4470
{4, 0.028, 0°, 80}	–0.0047	0.2035	-	-	0.2082
{4, 0.026, 2°, 200}	–0.1067	0.8373	-	-	0.9440
{4, 0.075, –1°, 150}	-	-	–0.1051	0.3206	0.4257
{4, 0.075, –1°, 80}	-	-	–0.0690	0.3380	0.4040
{4, 0.075, –1°, 200}	-	-	–0.8774	1.3096	2.1780

Figures 20(a) and (b) show the IWs of the A0 mode measured at $\mathbf{P}_{\mathrm{CHC}}\{4, 0.028, 0°, 80\}$ in the cases of narrowband and broadband. The corresponding arrival time-deviations of the IWs were determined with the reference signal u_{Ref} at 135° ($m_{\mathrm{Ref}} = 377$), the angle range, and the time windows as tabulated in Table 2 respectively. Then, the mean arrival time-deviations were determined as tabulated in Tables 6 and 7. The $\mu_{\Delta t}$ of the narrowband and broadband cases were found to be –0.0308 μs and –0.0047 μs with a $\sigma_{\Delta t}$ of –0.1732 μs and –0.2035 μs, respectively. It illustrated that the measurement at 80 mm has better wavefront characterization as compared to the previous case at 150 mm. Looking at Figs. 20(a) and (b), the IWs of the A0 mode were less contaminated than Figs. 19(a) and (b) as the reflected waves from the boundaries has yet arrived at 80 mm in all directions from 90° to 180° and not interfere with the IWs of the A0 mode. This is clearly illustrated in the UWI at the time instant of 84 μs for broadband case in Fig. 6(c).

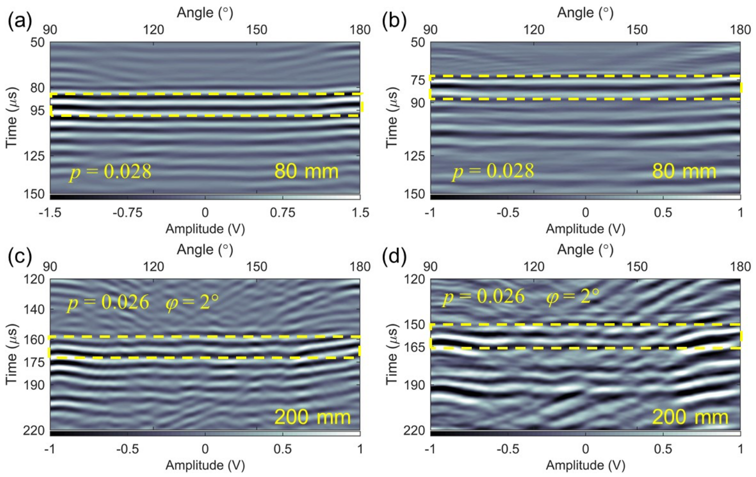

Figure 20. Ultrasonic responses with frequency bands of (a)(c) 140-160 kHz and (b)(d) 50-500 kHz ranging from 90° to 180° based on the cyclic-harmonic scanning curves at (a)(b) $\mathbf{P}_{\mathrm{CHC}}\{4, 0.028, 0°, 80\}$ and (c)(d) $\mathbf{P}_{\mathrm{CHC}}\{4, 0.026, 2°, 200\}$.

Figures 20(c) and (d) show the IWs of the A0 mode measured at the new updated parameter $\mathbf{P}_{\mathrm{CHC}}\{4, 0.026, 2°, 200\}$ after the updating process was performed in LUIS with the initial parameter at $\mathbf{P}_{\mathrm{CHC}}\{4, 0.028, 0°, 200\}$. It is noted that the elements p = 0.026 and φ = 2° were updated. Figures 20(c) and (d) show the IWs of the A0 mode for the narrowband and broadband cases respectively. The corresponding arrival time-deviations were also obtained with the reference signal at 135° ($m_{\mathrm{Ref}} = 943$), the angle range, and time windows as tabulated in Table 2.

At the R = 200 mm, the IWs were contaminated with a lot of interference from the reflected waves relative to the previous case of 80 mm. For this reason, the mean arrival time-deviation is higher than the cases at 80 mm and 150 mm as summarized in Tables 6 and 7, respectively. For the cases of narrowband and broadband, the interference of the reflected waves induced high standard deviations at 0.4058 μs and 0.8373 μs as shown in Figs. 20(c) and (d). The parameters obtained above were considered to characterize the IWs of the A0 mode in the region of non-fiber direction but not in the region of fiber direction. As a result, the characterization of the IWs of the A0 mode in the fiber direction region was investigated and discussed next.

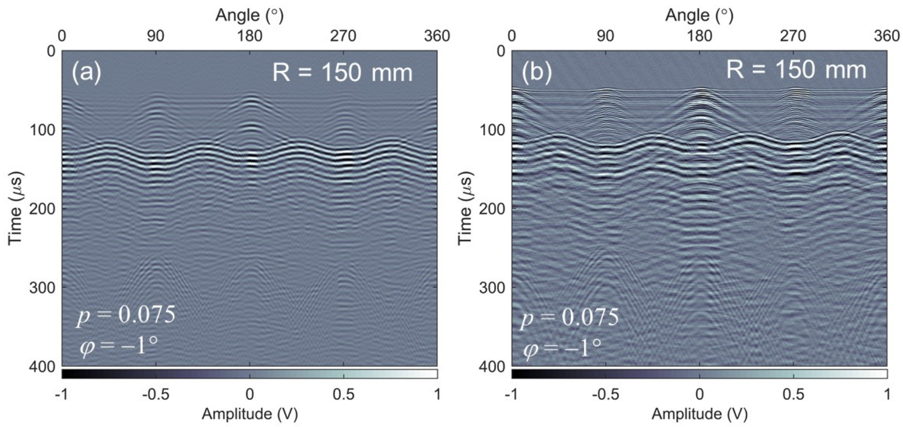

Figure 21. Ultrasonic responses with (a) 140-160 kHz and (b) 50-500 kHz based on the cyclic-harmonic scanning curves at $\mathbf{P}_{\text{CHC}}\{4, 0.075, -1°, 150\}$.

In Fig. 11(b), the ultrasounds were measured at the parameter $\mathbf{P}_{\text{CHC}}\{4, 0.07, 0°, 150\}$, and the patterns of the A0 mode IWs illustrated that the arrival time were about the same in the fiber direction region. For that, in this paper, the $\mathbf{P}_{\text{CHC}}\{4, 0.07, 0°, 150\}$ was chosen as the initial values for the LUIS to perform the updating process for the fiber direction region at 150 mm. As a result, the new parameter $\mathbf{P}_{\text{CHC}}\{4, 0.075, -1°, 150\}$ was obtained, and Fig. 17(b) shows the laser CHC scanning pattern. The corresponding ultrasonic signals were then measured and represented in PUWI as shown in Figs. 21(a) and (b) for narrowband and broadband cases, respectively.

Figures 22(a) and (b) show the zoomed PUWI of Figs. 21(a) and (b) from 135° to 225° for the narrowband and broadband cases, respectively. Repeating the same procedures from the S0 mode to Eqn. (4), the arrival time-deviations of both cases were obtained as shown in Figs. 22(c) and (d). Then, with Eqn. (5), the $\mu_{\Delta t}$ was determined for the narrowband and broadband cases, tabulated in Tables 6 and 7 accordingly. The $\mu_{\Delta t}$ of the narrowband and broadband cases were –0.0278 μs and –0.1051 μs, with a $\sigma_{\Delta t}$ of 0.2075 μs and 0.3206 μs, respectively. The parameter shows the ability to characterize the IWs of the A0 mode in the fiber direction region.

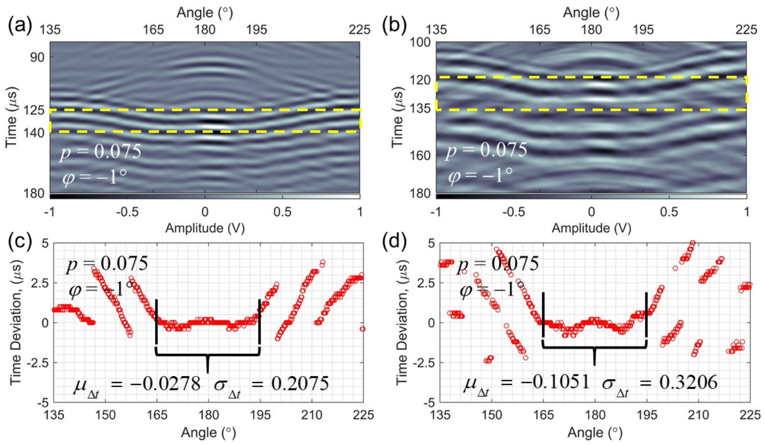

Figure 22. Ultrasonic responses with frequency bands of (a) 140-160 kHz and (b) 50-500 kHz ranging from 135° to 225°, and (c)(d) corresponding arrival time-deviations respectively, based on the cyclic-harmonic scanning curves at $\mathbf{P}_{\mathrm{CHC}}\{4, 0.075, -1°, 150\}$.

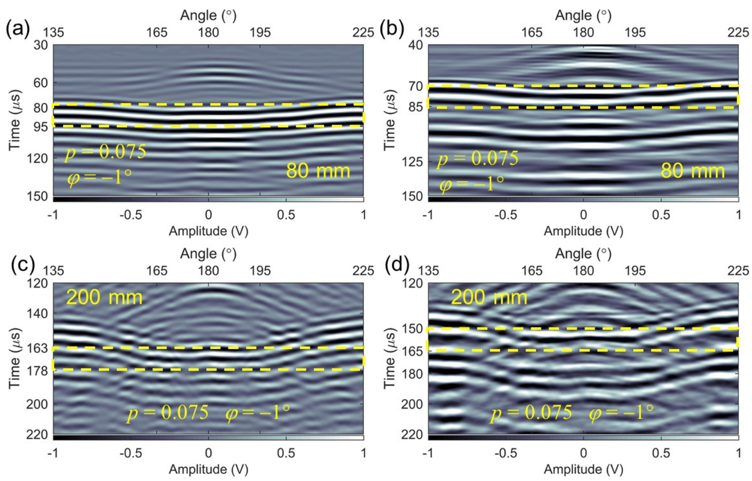

Figure 23. Ultrasonic responses with frequency bands of (a)(c) 140-160 kHz and (b)(d) 50-500 kHz ranging from 135° to 225° based on the cyclic-harmonic scanning curves at (a)(b) $\mathbf{P}_{\mathrm{CHC}}\{4, 0.075, -1°, 80\}$ and (c)(d) $\mathbf{P}_{\mathrm{CHC}}\{4, 0.075, -1°, 200\}$.

On the other hand, Figs. 23(a) and (b) show the measured ultrasound with the parameter $\mathbf{P}_{\mathrm{CHC}}\{4, 0.075, -1°, 80\}$ at the radius of 80 mm. As discussed in earlier results in Fig. 20, there was no interference of the IWs of the A0 mode from the reflected waves at 80 mm, as the reflected waves from the boundary of the plate need longer time to reach a radius of 80 mm from the center of the plate. Same in this case, the measured IWs of the A0 mode in fiber direction region were also not affected by the reflected waves. As a result, the mean arrival time-deviations for the narrowband and broadband cases were obtained to be –0.0376 μs and –0.0690 μs with standard deviations of 0.2059 μs and 0.3380 μs, respectively.

However, when the magnitude of R is increased, the IWs of the A0 mode are contaminated by the reflected wave from the S0 mode. For this reason, the mean arrival time-deviations at the radius of

200 mm (Tables 6 and 7) were highest among the other two cases (80 mm and 150 mm). In narrowband case, the mean arrival time-deviation is obtained –0.3377 μs with the standard deviation of 0.3769 μs, and in broadband case, the mean arrival time-deviation is –0.8774 μs and standard deviation of 1.3096 μs.

In both cases of S0 and A0 modes, the MADs of the non-fiber direction region were lesser than the MADs of the fiber direction region in both narrowband and broadband. This is because the change rate of the angular direction in the wavefront pattern was low in the non-fiber direction region as compared to the fiber direction region. In addition, the MADs in the case of narrowband were lesser than the MADs in the case of broadband in both fiber and non-fiber directions regions. It is because the proposed method was sensitive to the complexity of the wavefront pattern. Since, in the case of broadband, the spatial wavefront of the ultrasound is more complex with multi-mode and multi-frequency components than the case of narrowband, it is difficult for the laser cyclic-harmonic curve scan to characterize the complex wavefronts.

The proposed method was also dependent on the purity of the wavefront pattern. As seen in the case of the A0 mode, as the testing radius increased, the MAD was increased because the IWs of the A0 mode interfered with the reflected waves at further distances from the source. Beyond that, it was also shown that the dispersive nature of the A0 mode would cause an increase in MAD at the same parameters' values, e.g. at the radii of 80 mm and 150 mm in Tables 6 and 7.

3.3.2 Reflected Wavefront Characterization

As demonstrated in previous subsection 3.3, the proposed method was reasonably capable of characterizing the incident wavefronts of the S0 and A0 modes for the aluminum and cross-ply CFRP plates. In the following subsection, the feasibility of the proposed method is further tested on the reflected waves of the aluminum and cross-ply CFRP plates.

Aluminum Plate

Figures 24(a) and (b) show spatial ultrasonic wavefront images in a 2-D spatial plane at different time-instants 85 μs and 132.8 μs. The red-dotted curves on the reflected wavefronts at various times show the similar curve pattern in hyperbolic curve as discussed in previous subsection 3.2.1. Figures 24(a) and (b) indicate that the same reflected wavefronts propagated through two local points (180°, 85) and (137°, 131) at two different time instants of 85 μs and 132.8 μs, respectively. The corresponding ultrasonic signals, $u_1(180°, 85, t)$ and $u_2(137°, 131, t)$, were considered and the responses to the time history waves were plotted as shown in Figs. 24(c). By looking at the boxes A and B as shown on the right side of the Fig. 24(c), the two signals were approximately in phase from 84 μs to 88 μs and from 130 μs to 134 μs respectively.

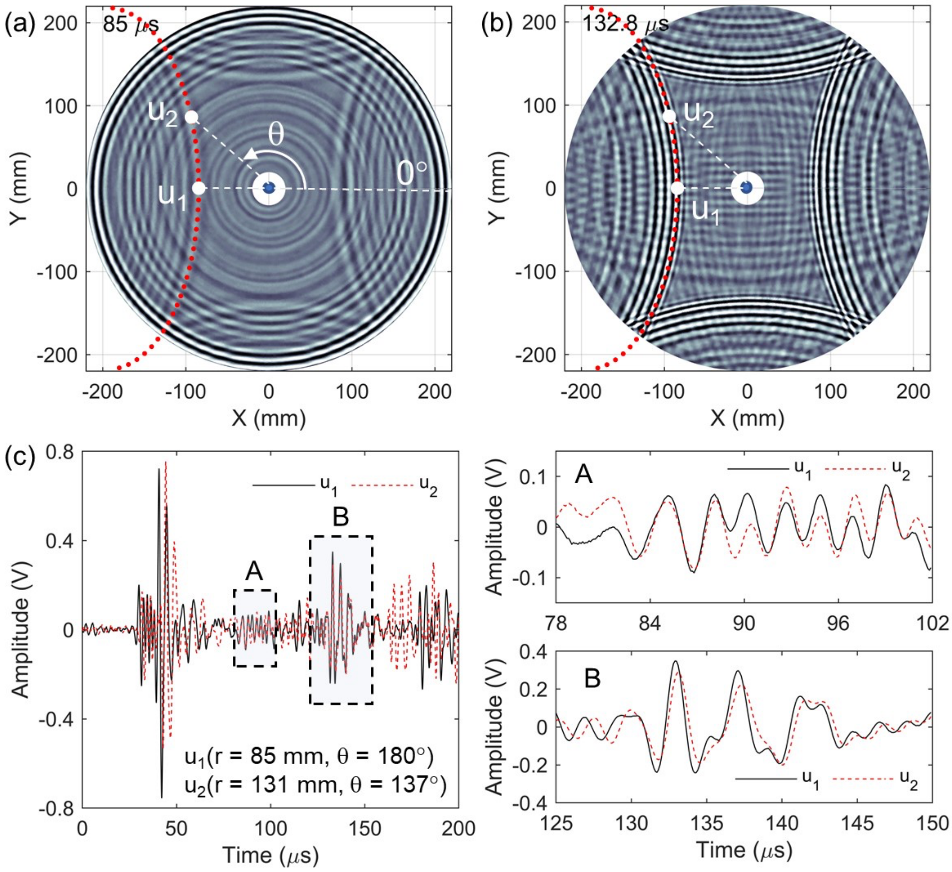

Figure 24. Aluminum plate UWI at (a) 85 μs, (b) 132.8 μs, and (c) local ultrasonic signals $u_1(180°, 85, t)$ and $u_2(137°, 131, t)$.

It infers that the reflected wavefronts may be characterized by obtaining all the corresponding local points (liked u_1 and u_2) that are positioned on the coordinates of the same wavefront. For this reason, as referred to in the previous subsection 3.2.2, the characterized curve (hyperbolic curve) was obtained to characterize the reflected wavefronts of the aluminum and cross-ply CFRP plates are discussed next for Process 2.

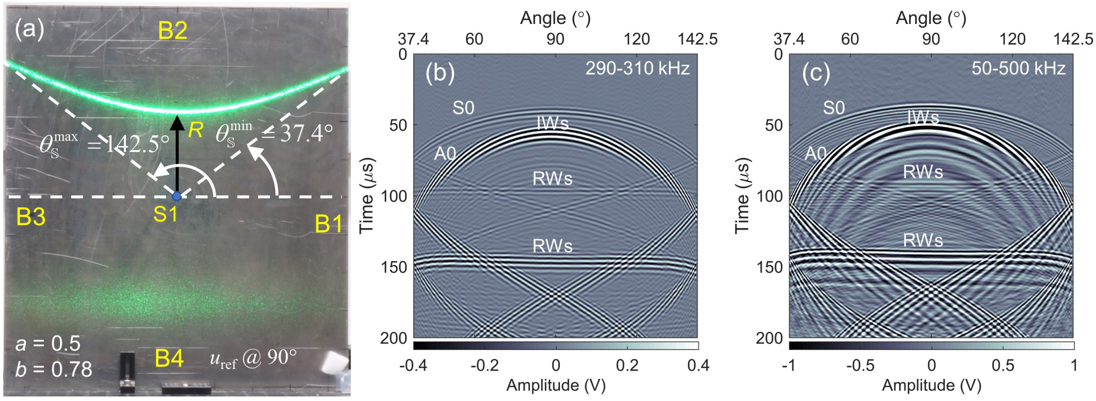

Figure 25. (a) Laser hyperbolic scanning pattern with parameter $\mathbf{P}_{\mathrm{H}}\{0.5, 0.78, 90°, 0\}$ on aluminum plate and corresponding ultrasounds in PUWI with frequency ranges of (b) 290-310 kHz and (b) 50-500 kHz.

In Process 1, the characterized curve was obtained based on the spatial ultrasonic wavefront image in Fig. 5(b) and the corresponding parameters and scale factors were estimated at $\mathbf{P}_{\mathrm{H}}\{0.5, 0.68, 90°, 0\}$. As for that, the LUIS performed the laser hyperbolic scan at the initial values of $\mathbf{P}_{\mathrm{H}}\{0.5, 0.68, 90°, 0\}$. Upon completion of the updating process in Process 2, the updated parameter was obtained at $\mathbf{P}_{\mathrm{H}}\{0.5, 0.78, 90°, 0\}$. Throughout the scanning process, the laser scanner mirror maneuvered the pulsed laser beam with the coordinates generated in $\mathbb{S}$-plane based on the $\mathbf{P}_{\mathrm{H}}\{0.5, 0.78, 90°, 0\}$ as shown in Fig. 25(a). Since the zero degree was assigned at the line y = 0 with the condition of $0 \le x \le w_x$ toward to the boundary B1 (Fig. 25(a)), these $\theta_{\mathbb{S}}^{\min}$ and $\theta_{\mathbb{S}}^{\max}$ were then determined at 37.4° and 142.5° respectively, from Eqn. (12) with the consideration of the rotation angle Ω of 90° in Eqn. (11) and the interval angle of 0.04°. The radius (R) was calculated at 127 mm from the center (Fig. 25(a)) based on the expression $aw_x + A_{\text{offset}}$ in section 3.2.2.

Figures 25(b) and (c) show the PUWIs based on the $\mathbf{P}_{\mathrm{H}}\{0.5, 0.78, 90°, 0\}$ for the narrowband (290-310 kHz) and broadband (50-500 kHz) cases, respectively. Both PUWIs show the IWs of the S0 and A0 modes were arrived at various times. Note, on the other hand, that the wavefronts of the reflected waves from the boundary B2 had arrived at the same times and formed lines-liked, denoted as RWs in Figs. 25(b) and (c). Besides than the RWs propagating from B2, the PUWI indicates also the other reflected waves propagating from the boundaries B1 and B3.

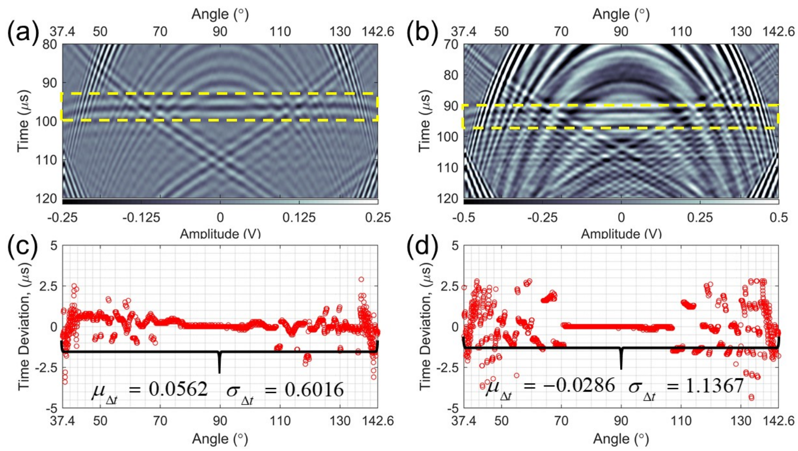

Figure 26. Zoomed PUWIs with frequency ranges of 290-310 kHz and (b) 50-500 kHz, and (c)(d) corresponding arrival time-deviations respectively for RWs due to S0 mode at $\mathbf{P}_{\mathrm{H}}\{0.5, 0.78, 90°, 0\}$.

Figures 26(a) and (b) show the zoomed PWUI of Figs 25(b) and (c) for the narrowband and broadband respectively. The yellow boxes in Figs. 26(a) and (b) show the RWs propagating from the boundary B2 after the IWs of S0 mode struck at the B2. The measurement of the ultrasound based on $\mathbf{P}_{\mathrm{H}}\{0.5, 0.78, 90°, 0\}$ demonstrated the ability to characterize the RWs from the B2, and these RWs were denoted as S_{B2} in this paper. Figures 26(c) and (d) show the arrival time-deviations obtained with the reference signal at 90° ($m_{\mathrm{Ref}} = 1315$) for both narrowband and broadband, respectively. Then, the time windows were set from 92 μs ($k_{\min} = 460$) to 100 μs ($k_{\max} = 500$) for the case of narrowband and from 90 μs ($k_{\min} = 450$) to 95 μs ($k_{\max} = 475$) for the case of broadband. Table 8 shows $\mu_{\Delta t}$ was determined to be 0.0562 μs with a $\sigma_{\Delta t}$ of 0.6026 μs for the narrowband case, and –0.0286 μs with a $\sigma_{\Delta t}$ of 1.1367 μs for the broadband case.

Both mean arrival time-deviations were close to zero, but both MADs were higher than the previous IWs cases. It is because their standard deviations were high, especially the arrival time-deviations in the directions 37.4° to 75° and 110° to 142.6°, as shown in Figs. 26(c) and (d). By referring to the PUWI in Figs. 26(a) and (b), there was a lot of interference from another boundary between S_{B2} and other RWs. Despite this interference, the visibility of the S_{B2} pattern was still clearly illustrated in the PUWI. Hence, the laser hyperbolic scan at the $\mathbf{P}_{\mathrm{H}}\{0.5, 0.78, 90°, 0\}$ was still able to characterize the RWs in the directions ranging from 70° to 110° in this paper.

Table 8. Summary of mean arrival time-deviation for characterization of RWs due to S0 and A0 modes using laser hyperbolic scanning method with narrowband of 290 kHz-310 kHz and broadband 50 kHz-500 kHz.

$\mathbf{P}_{\mathrm{H}}\{a, b, \Omega, A_{\mathrm{offset}}\}$	Narrowband	Broadband

	$\mu_{\Delta t}$	$\sigma_{\Delta t}$	MAD (μs)	$\mu_{\Delta t}$	$\sigma_{\Delta t}$	MAD (μs)
S0 Mode						
{0.5, 0.78, 90°, 0}	0.0562	0.6026	0.6588	−0.0286	1.1367	1.1653
{0.5, 0.9, 132°, 80}	-	-	-	-	-	-
A0 Mode						
{0.5, 0.78, 90°, 0}	0.0519	0.4894	0.5413	−0.0527	0.8526	0.9053
{0.5, 0.9, 132°, 80}	0.1018	0.3870	0.4888	0.1218	0.3209	0.4427

Figures 27(a) and (b) show another RW A0 mode from boundary B2, denoted as A_{B2}. The arrival time-deviations were obtained with the same settings in the case of S_{B2}, except the time windows. The time windows were set to 142 μs ($k_{min} = 710$) to 150 μs ($k_{max} = 750$) for the case of narrowband and 138 μs ($k_{min} = 690$) and 148 μs ($k_{max} = 740$) for the case of broadband as shown in Figs. 27(c) and (d) respectively. The mean arrival time-deviations for the narrowband and broadband cases were found to be 0.0519 μs with a $\sigma_{\Delta t}$ of 0.4894 μs and −0.0527 μs with a $\sigma_{\Delta t}$ of 0.8526 μs, as tabulated in Table 8. The MADs of A_{B2} demonstrate greater accuracy than the MADs of S_{B2}. This is because the A_{B2} had less interference than the S_{B2} case in the directions 37.4° to 75° and 110° to 142.6°.

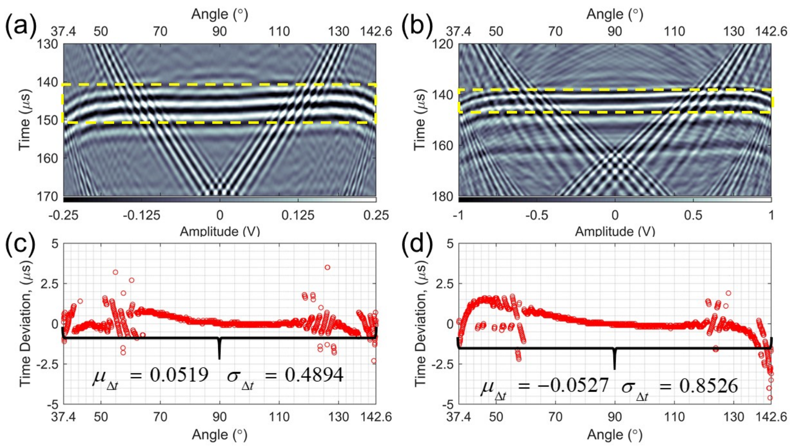

Figure 27. Zoomed PUWIs with frequency ranges of 290-310 kHz and (b) 50-500 kHz, and (c)(d) corresponding arrival time-deviations respectively for RWs due to A0 mode at $\mathbf{P}_{\mathrm{H}}\{0.5, 0.78, 90°, 0\}$.

Next, the RWs from the corner of the aluminum plate were considered and characterized. In the previous Process 1, the characterized curve with the parameter of $\mathbf{P}_{\mathrm{H}}\{0.5, 1, 132°, 80\}$ was determined for the RWs propagating from the corner E2 as shown in Fig. 5(c)). The LUIS then performed the laser hyperbolic scan at an angle interval of 0.04° with this parameter as an initial setting. Figure 28(a) shows the laser hyperbolic scanning curve of the updated parameter of $\mathbf{P}_{\mathrm{H}}\{0.5, 0.9, 132°, 80\}$ on the aluminum plate from $\theta_{\mathbb{S}}^{\min} = 98.9°$ ($m_{\min} = 1$) to $\theta_{\mathbb{S}}^{\max} = 161.6°$ ($m_{\max} = 1568$). Since the aluminum plate was rectangular, the angle at the corner E2 was at 132° ($m_{\mathrm{Ref}} = 830$) instead of 135° and the ultrasonic signal at 132° was used as the reference signal u_{Ref}.

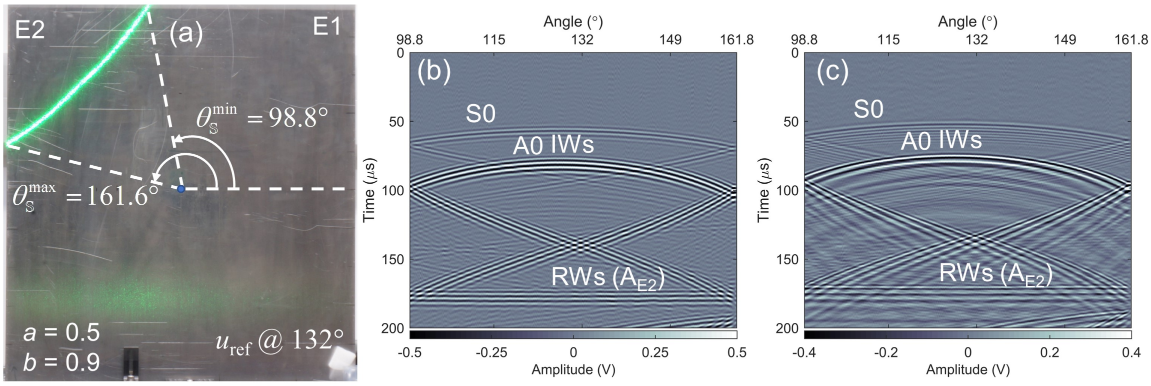

Figure 28. (a) Laser hyperbola scanning pattern with parameter $\mathbf{P}_{\mathrm{H}}\{0.5, 0.9, 132°, 80\}$ on aluminum plate and corresponding ultrasounds in PUWI with frequency ranges of (b) 290-310 kHz and (b) 50-500 kHz.

Figures 28(b) and (c) show the PUWIs for the cases of narrowband and broadband respectively. It notes that the RWs, denoted as A_{E2}, were obtained, generated at corner E2 after the IWs of A0 mode impinged there. It was noted, however, that the RWs propagating from E2 due to S0 mode were not seen. The low signal-to-noise ratio of the IWs of the S0 mode was suspected to have significantly further diminished after hitting corner E2. As a result, the characterization of the RWs (A_{E2}) was only tested in this paper.

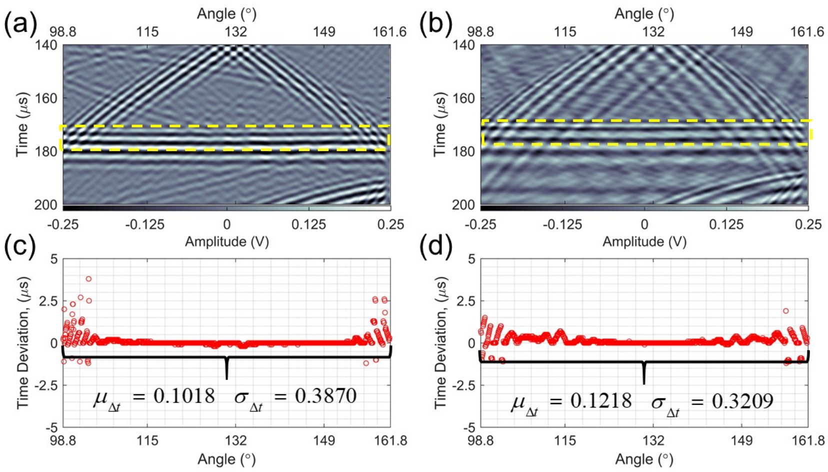

Figure 29. Zoomed PUWIs with frequency ranges of 290-310 kHz and (b) 50-500 kHz, and (c)(d) corresponding arrival time-deviations respectively for RWs due to A0 mode at $\mathbf{P}_{\mathrm{H}}\{0.5, 0.9, 132°, 80\}$.

Figures 29(a) and (b) show the zoomed-in PUWI of Figs. 28(b) and (c), respectively. The arrival time-deviations were then obtained with the time windows of 172 μs ($k_{\min} = 860$) to 177 μs ($k_{\max} = 880$) for both narrowband and broadband as shown in Figs. 29(c) and (d). As tabulated in Table 8, the $\mu_{\Delta t}$ were calculated to be 0.1018 μs with a $\sigma_{\Delta t}$ of 0.3870 μs for the narrowband case, and to be 0.1218 μs with a $\sigma_{\Delta t}$ of 0.3209 μs for the broadband case. The corresponding MADs for the cases of narrowband and broadband were obtained at 0.4888 μs and 0.4427 μs respectively. Among the results tabulated in Table 8, the characterization of the RWs from the corner E2 is more accurate than the RWs from the boundary B2. It is because of the high interference of B2 over the RWs compared to the E2.

CFRP Plate

Next, the laser hyperbolic scan was further tested to the cross-ply CFRP plate. Based on Fig. 6(c), the characterized curve (hyperbolic curve) was determined at the parameter of $\mathbf{P}_{\mathrm{H}}\{0.5, 0.35, 180°, 20\}$ in Process 1. Subsequently, using $\mathbf{P}_{\mathrm{H}}\{0.5, 0.35, 180°, 20\}$ as an initial setting, the LUIS performed the laser hyperbolic scan and the updated parameter was obtained at $\mathbf{P}_{\mathrm{H}}\{0.5, 0.4, 180°, 20\}$. Figure 30(a) shows the laser hyperbolic scanning curve from $\theta_{\mathbb{S}}^{\min} = 148.5°$ to $\theta_{\mathbb{S}}^{\max} = 211.5°$ at $\mathbf{P}_{\mathrm{H}}\{0.5, 0.4, 180°, 20\}$. Figures 30(b) and (c) show the PUWIs for the narrowband and broadband cases, respectively. Looking at the Fig. 6(c), the RWs were generated and they propagated in the directions of fiber. The IWs of the S0 mode were suspected as the source of the RWs generation since the S0 mode traveled faster than the A0 mode as shown in Fig. 6(c). In addition, the spatial ultrasonic wavefront image at 84 μs, as shown in Fig. 6(c), displays that the RWs were interfered with the IWs of the S0 mode, but not with the IWs of the A0 mode. Consequently, the updated parameter $\mathbf{P}_{\mathrm{H}}\{0.5, 0.4, 180°, 20\}$ was used to characterize the RWs as induced by the IWs of the S0 mode.

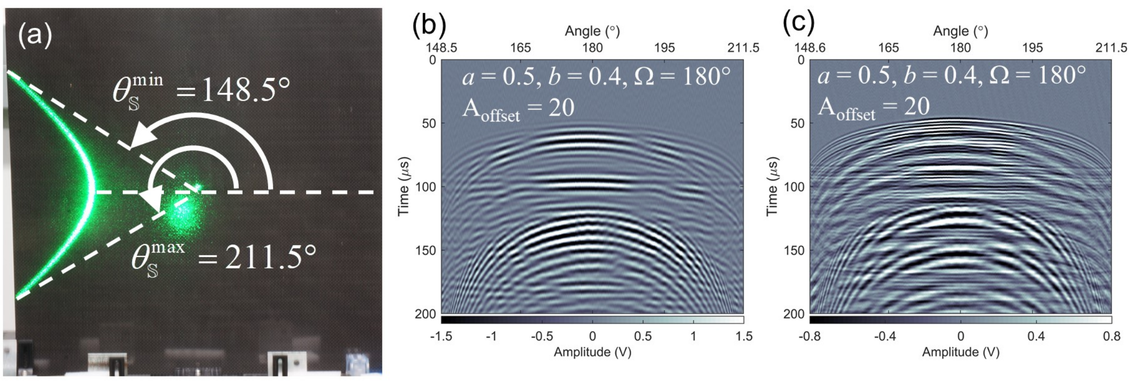

Figure 30. (a) Laser hyperbola scanning pattern with parameter $\mathbf{P}_{\mathrm{H}}\{0.5, 0.4, 180°, 20\}$ on aluminum plate and corresponding ultrasounds in PUWI with frequency ranges of (b) 140-160 kHz and (b) 50-500 kHz.

Figures 31(a) and (b) show the zoomed PUWIs of Figs. 30 (a) and (b) respectively. Figures 31(c) and (d) show that the arrival time-deviations were obtained with the reference signal at 180° ($m_{\mathrm{Ref}} = 789$). In the narrowband case, the time window was set to from 90 μs ($k_{\min} = 450$) to 102 μs ($k_{\max} = 510$), and in the broadband case the time window was set to 78 μs ($k_{\min} = 390$) to 96 μs ($k_{\max} = 480$). Although the lines-liked of the RWs can be seen in Figs. 31(a) and (b), but the results of the arrival time-deviations showed that the parameter barely characterized the RWs correctly, approximately to zero, in the fiber direction region ($165° \le \phi_{\mathbb{S}} \le 195°$) for both cases.

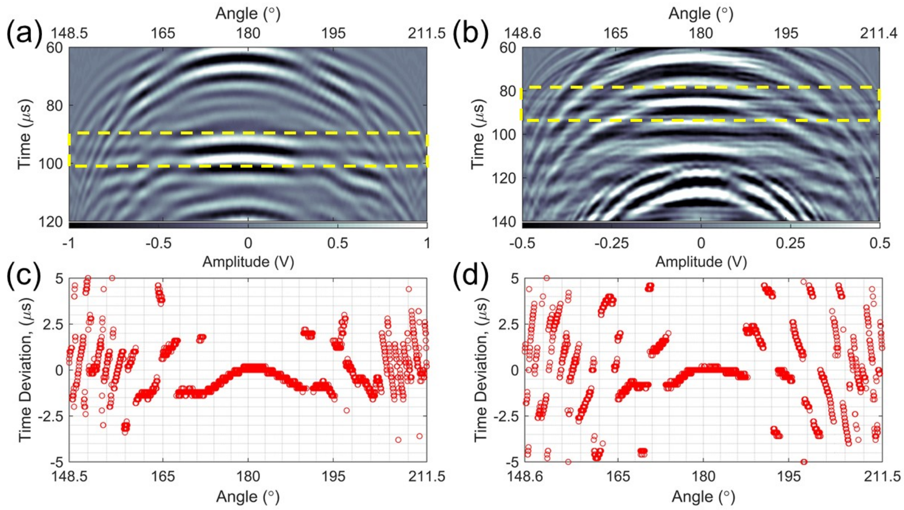

Figure 31. Zoomed PUWIs with frequency ranges of 140-160 kHz and (b) 50-500 kHz, and (c)(d) corresponding arrival time-deviations respectively for RWs due to S0 mode at $\mathbf{P}_{\mathrm{H}}\{0.5, 0.4, 180°, 20\}$.

4. CONCLUSION

In this paper, a new spatial ultrasonic wavefront characterization method based on parametric curve equation was proposed and performed to overcome the drawbacks of initial work [9] to accelerate the laser ultrasonic inspection time by optimizing the spatial scanning pattern. The proposed method was tested on aluminum and cross-ply CFRP plates to characterize the spatial incident and reflected wavefronts of the plates. In this paper, the non-fiber direction region ($105° \le \phi_{\mathbb{S}} \le 165°$) and the fiber direction region ($165° \le \phi_{\mathbb{S}} \le 195°$) of the cross-ply CFRP plate were considered in the test. Then, the performance of the wavefront characterization was evaluated based on the maximum absolute deviation of the mean arrival time-deviation. The results are summarized as follows:

- Using ultrasonic images, the incident and reflected wavefronts on rectangular boundary specimens were identified and shown to have strong correlation to fundamental parametric curves. The circular curve for the aluminum plate and the cyclic-harmonic curve for cross-ply CFRP plate were identified in the incident wavefront, and the hyperbolic curve for both plates was identified in reflected wavefront.
- The laser circle scan showed the ability to characterize the incident wavefronts of the S0 and A0 modes of the aluminum plate with the parametric circle equation. The characterization efficiency was determined at the lowest maximum absolute deviations of 0.2562 μs for S0 mode and 0.4742 μs for A0 mode.
- The laser cyclic-harmonic curve scan with the parametric cyclic-harmonic curve equation showed the ability to characterize the incident wavefronts of the S0 and A0 modes at various radii in the regions of fiber and non-fiber directions. It showed greater characterization efficiency in the non-fiber direction regions of both modes using a narrowband excitation. The efficiency of the wavefront characterization was dependent on the change rate of the angular direction, simplicity, and purity in the wavefront pattern.
- The proposed method showed the high versatility and spatial resolution features that scanning curve can be easily modified by changing the parameter values to increase the efficiency of the characterization, as proven in Fig. 14. In addition, the suspected local fiber stacking variations were detected in the CFRP plate in Fig. 14 due to these novel features in the laser cyclic-harmonic curve scan.
- The laser hyperbolic scan with the parametric hyperbolic curve equation showed the ability to characterize the reflected wavefronts, either from the aluminum plate boundary or corner, that due to the S0 mode and the A0 mode. In the case of narrowband input, it showed greater characterization efficiency than the case of broadband input. Nevertheless, in both cases it has high MAD because of the interference from the other reflected wavefronts from other boundaries and corners.
- The laser hyperbolic curve scan showed ability to parameterize the reflected wavefronts in the CFRP plate. However, the cross-correlation method was unable to quantify the performance of the technique because the multiple waves superimposed made the images too complex to parameterize in a fundamental curve.
- In the case of the aluminum plate, the laser hyperbolic curve scan showed the ability to identify when and localize where the reflected waves were crossed to each other in the PUWI. This feature may provide useful information in a sparse sensing approach for damage detection, where the positioning of the sensor can be optimized by avoiding undesirable locations that are not helpful in the overall detection performance.

The summary above gives a clear picture of the feasibility of the proposed method, but there is plenty of room for further enquiry and development. First, the temporal cross-correlation technique used in this paper should be improved or reassessed using another robust technique to quantify the performance of the wavefront characterization. This is because the cross-correlation coefficient has a strong relationship to the selected reference signal. Therefore, if the reference signal is distinct from the test signal, it suffers in generating useful results. As illustrated in the case of the A0 mode (Fig. 9(c)), the selected reference signal (180°) was different from the test signal because it was contaminated by the reflected wave. Second a wave decomposition technique is required to improve the quality of the desired wavefront by isolating or filtering the superimposed multiple wavefronts. Lastly, the repeatability of the proposed method must be evaluated with multiple specimens with the same controlled manufacturing configurations.

Acknowledgement

The authors acknowledge funding from UC Office of the President for support of this work.

References

[1] Y.-K. An, B. Park, and H. Sohn, "Complete noncontact laser ultrasonic imaging for automated crack visualization in a plate," *Smart Materials and Structures,* vol. 22, no. 2, p. 025022, 2013.

[2] E. B. Flynn, S. Y. Chong, G. J. Jarmer, and J.-R. Lee, "Structural imaging through local wavenumber estimation of guided waves," *Ndt & E International,* vol. 59, pp. 1-10, 2013.

[3] D. Girolamo, H.-Y. Chang, and F.-G. Yuan, "Impact damage visualization in a honeycomb composite panel through laser inspection using zero-lag cross-correlation imaging condition," *Ultrasonics,* vol. 87, pp. 152-165, 2018.

[4] J.-R. Lee, S. Y. Chong, H. Jeong, and C.-W. Kong, "A time-of-flight mapping method for laser ultrasound guided in a pipe and its application to wall thinning visualization," *NDT & E International,* vol. 44, no. 8, pp. 680-691, 12// 2011.

[5] S. Y. Chong and M. D. Todd, "Dispersion curve estimation via a spatial covariance method with ultrasonic wavefield imaging," *Ultrasonics,* vol. 89, pp. 46-63, 2018/09/01/ 2018.

[6] S. Y. Chong, J. J. Victor, and M. D. Todd, "Full-field ultrasonic inspection for a composite sandwich plate skin-core debonding detection using laser-based ultrasonics," in *SPIE Smart Structures and Materials + Nondestructive Evaluation and Health Monitoring*, 2017, vol. 10170, p. 10: SPIE.

[7] Z. Tian, L. Yu, and C. Leckey, "Delamination detection and quantification on laminated composite structures with Lamb waves and wavenumber analysis," *Journal of Intelligent Material Systems and Structures,* vol. 26, no. 13, pp. 1723-1738, 2015.

[8] B. Park, H. Sohn, and P. Liu, "Accelerated noncontact laser ultrasonic scanning for damage detection using combined binary search and compressed sensing," *Mechanical Systems and Signal Processing,* vol. 92, pp. 315-333, 2017/08/01/ 2017.

[9] S. Y. Chong and M. D. Todd, "Statistical damage detection based on full-field covariance of circumferential scan ultrasonic measurement," in *Health Monitoring of Structural and Biological Systems XII*, 2018, vol. 10600, p. 106002J: International Society for Optics and Photonics.

[10] J. E. Michaels, "Ultrasonic wavefield imaging: Research tool or emerging NDE method?," *AIP Conference Proceedings,* vol. 1806, no. 1, p. 020001, 2017.

[11] J. E. Michaels, "Ultrasonic Wavefield Imaging," in *Handbook of Advanced Non-Destructive Evaluation*, N. Ida and N. Meyendorf, Eds. Cham: Springer International Publishing, 2018, pp. 1-32.

[12] S. Y. Chong and J.-R. Lee, "Development of laser ultrasonic propagation imaging system with twenty-kilohertz scanning frequency for nondestructive evaluation applications," *P. of Advances in Structural Health Management and Composite Structures,* vol. 1, pp. 181-184, 2014.

[13] H.-J. Shin and J.-R. Lee, "Development of a long-range multi-area scanning ultrasonic propagation imaging system built into a hangar and its application on an actual aircraft," *Structural Health Monitoring,* vol. 16, no. 1, pp. 97-111, 2017.

[14] D. Mascareñas, S. Y. Chong, G. Park, J. Lee, and C. Farrar, "Application of compressed sensing to 2-D ultrasonic propagation imaging system data," in *6th European Workshop on Structural Health Monitoring*, 2012, pp. 1-8.

[15] T. Di Ianni, L. De Marchi, A. Perelli, and A. Marzani, "Compressive sensing of full wave field data for structural health monitoring applications," *IEEE transactions on ultrasonics, ferroelectrics, and frequency control,* vol. 62, no. 7, pp. 1373-1383, 2015.

[16] O. Mesnil and M. Ruzzene, "Sparse wavefield reconstruction and source detection using compressed sensing," *Ultrasonics,* vol. 67, pp. 94-104, 2016.

[17] J. B. Harley and C. C. Chia, "Statistical partial wavefield imaging using Lamb wave signals," *Structural Health Monitoring,* vol. 0, no. 0, p. 1475921717727160, 2017.

[18] J. B. Harley and J. M. F. Moura, "Sparse recovery of the multimodal and dispersive characteristics of Lamb waves," *The Journal of the Acoustical Society of America,* vol. 133, no. 5, pp. 2732-2745, 2013.

[19] R. Remi and K. Schnass, "Dictionary Identification - Sparse Matrix-Factorization via L1-Minimization," *IEEE Transactions on Information Theory,* vol. 56, no. 7, pp. 3523-3539, 2010.

[20] J. W. Rutter, *Geometry of curves*. Chapman and Hall/CRC, 2000.

[21] C. Zwikker, *The advanced geometry of plane curves and their applications*. Courier Corporation, 2011.

[22] T. Lewiner, J. D. Gomes, H. Lopes, and M. Craizer, "Curvature and torsion estimators based on parametric curve fitting," *Computers & Graphics,* vol. 29, no. 5, pp. 641-655, 2005/10/01/ 2005.

[23] M. Grossman, "Parametric curve fitting," *The Computer Journal,* vol. 14, no. 2, pp. 169-172, 1971.